이학박사학위논문

Heterogeneous Dynamics and Electrolyte Applications of Ionic Liquids

이온성 액체의 동력학적 불균일성과 전해질로써 응용

2016년 2월

서울대학교 대학원
화학부 물리화학 전공
박 상 원

Heterogeneous Dynamics and Electrolyte Applications of Ionic Liquids

이온성 액체의 동력학적 불균일성과 전해질로써 응용

지도교수 정 연 준

이 논문을 이학박사 학위논문으로 제출함
2016년 1월

서울대학교 대학원
화학부 물리화학 전공
박 상 원

박상원의 이학박사 학위논문을 인준함
2015년 12월

위 원 장	석 차 옥	(인)
부위원장	정 연 준	(인)
위 원	이 상 엽	(인)
위 원	성 봉 준	(인)
위 원	심 영 선	(인)

Heterogeneous Dynamics and Electrolyte Applications of Ionic Liquids

by

Sang-Won Park

Supervised by

Professor **YounJoon Jung**

A Dissertation
Submitted to the Faculty of
Seoul National University
in Partial Fulfillment of
the Requirements for the Degree of
Doctor of Philosophy

February 2016

Department of Chemistry
Graduate School
Seoul National University

Abstract

Ionic liquids (ILs), or room-temperature ionic liquids (RTILs), have attracted considerable attention from both academia and industry, due to their peculiar properties and wide applicabilities as electrolytes. In this dissertation, we study both their dynamic properties as a glass-forming liquid and the applicability as electrolytes in supercapacitors via molecular dynamics simulations.

In the first part, we study how dynamic heterogeneity in ionic liquids is affected by the length scale of structural relaxation and the ionic charge distribution by adopting two differently charged models of ionic liquid and their uncharged counterpart. In one model of ionic liquid, the charge distribution in the cation is asymmetric, and in the other it is symmetric, while their neutral counterpart has no charge with the ions. It is found that all the models display heterogeneous dynamics, exhibiting subdiffusive dynamics and nonexponential decay of structural relaxation. We investigate the lifetime of dynamic heterogeneity, τ_{dh}, in these systems by calculating the three-time correlation functions to find that τ_{dh} has in general a power-law behavior with respect to the structural relaxation time, τ_α: $\tau_{\mathrm{dh}} \propto \tau_\alpha^{\zeta_{\mathrm{dh}}}$. Although the dynamics of the asymmetric-charge model is seemingly more

heterogeneous than that of the symmetric-charge model, the exponent is found to be similar, $\zeta_{\mathrm{dh}} \approx 1.2$, for all the models studied in this work. The same scaling relation is found regardless of interactions, *i.e.*, with or without Coulomb interaction, and it holds even when the length scale of structural relaxation is long enough to become the Fickian diffusion. This fact indicates τ_{dh} is a distinctive time scale from τ_α, and the dynamic heterogeneity in these systems is mainly affected by the short-range interaction and the molecular structure.

In the second part, we study electric double layer capacitors (EDLCs) in the parallel plate configuration of graphene oxide (GO). Electric double layer capacitors (EDLCs), or supercapacitors, offer high power densities and moderate energy densities for energy storage applications. The oxidation range of electrode is varied from 0% (pure graphene) to 100% (fully oxidized GO) by decorating graphene surface with hydroxyl groups. Two different electrolytes, 1-ethyl-3-methylimidazolium tetrafluoroborate ($\mathrm{EMI}^+\mathrm{BF}_4{}^-$) as an ionic liquid (IL) and its 1.3 M solution in acetonitrile as an organic electrolyte (OE), are considered. While the area-specific capacitance tends to decrease with increasing electrode oxidation for both electrolytes, its details show interesting differences between OE and IL, including the extent of decrease. The difference in the capacitances between them is pronounced at the cathode of low oxidation, and the anion is identified as the key species in screening ability that makes the difference in the capacitance. Hydrogen bonding between the hydroxyl groups of GO and the anions is the major factor that yields this unexpected result. For detailed insight into these differences, the screening mechanisms of electrode charges by electrolytes and their variations with electrode oxidation are analyzed with special attention

paid to the aspects shared by and the contrasts between IL and OE.

Keywords: ionic liquids, dynamic heterogeneity, glassy dynamics, electric double layer, supercapacitor, graphene oxide

Student Number: 2008-20323

Contents

List of Figures

List of Tables

Chapter 1

Overview

Ionic liquids (ILs), or room-temperature ionic liquids (RTILs), are a new class of organic molecules that are composed of cations and anions and usually have melting points near room temperature. Because the components of ILs can be varied in a great number of combinations, one can in principle design appropriate IL solvents for specific purposes in applications. Due to their high polarity, ILs are also able to dissolve a wide range of different solute molecules, so they can be used in extracting carbon dioxide, for example. Because ILs have a negligible vapor pressure due to their strong Coulomb attraction, they are considered to be "green" alternatives to typical volatile, inflammable and toxic organic solvents.[1,2]

ILs are mostly composed of bulky, asymmetric cations and small, symmetric anions. Their size disparity as well as structural complexity inhibits crystallization and helps them to remain in liquid states, in spite of the strong Coulomb attraction. Due to these reasons, they exhibit different dynamical behaviors from normal liquids. The unique property is represented by glassy dynamics, which has been studied very well in glass-forming liq-

uids, such as supercooled liquids and polymer melts. Due to their complex molecular structure, ILs also have various interactions, *e.g.*, electrostatic interaction, cation-π interaction, π-π interaction, hydrogen bonding, *etc.* The bulky structure also enables them very stable with a wide range of thermal and electrochemical window. ILs thus have been widely used as electrolytes in supercapacitors and solar cells.[2]

Currently ILs are attracting significant interest both from academia and industry due to their unique properties and possible applications in diverse areas, as presented above, and both aspects are studied in this dissertation. A property arousing the fundamental curiosity towards ILs is glassy dynamics, represented by dynamic heterogeneity, and one of the promising applicabilities of ILs is electrolytes in supercapacitors.

1.1 Heterogeneous dynamics of ionic liquids

In Part I, we study the dynamic heterogeneity of ILs with simple toy models via molecular dynamics simulation.[3,4] ILs exhibit slow dynamical behavior that are typically characterized by subdiffusivity and nonexponential relaxation as in glass-forming liquids. The overall nonexponential dynamics in glass forming liquids is ascribed to the superposition of exponential relaxations with different relaxation times, or heterogeneous dynamics, which is the case with glass-forming liquids including ILs.[5–56] Time and length scale of dynamic heterogeneity is important for obtaining microscopic understanding of dynamical behavior of liquids.[20–41] and polymer melts,[50–53] Despite such interest, the dynamic length and time scales of ILs and the relation between them have not been thoroughly understood.[19]

We focus on the issue of the correlation between the local charge distribution of cations and the dynamic heterogeneity of ILs by investigating the lifetimes of dynamic heterogeneity by calculating their three-time correlation functions (3TCFs). The validity of the 3TCF as a quantity measuring the dynamic heterogeneity is examined from the relation between the time scale of the 3TCFs and that of the two-point correlation functions, such as the structural relaxation and the relaxation of rotational motion. Moreover, we explore breakdown of the Stokes-Einstein relation, one of the well-known features found in liquid systems showing glassy dynamics. The dependence of the dynamic heterogeneity time scale on the length scale of the structural relaxation time is explored to show that it is a time scale distinct from that of diffusion.

1.2 Electrolyte applications of ionic liquids

In Part II, we study the electric double layer capacitors (EDLCs) having ionic liquid electrolytes, one of the applicabilities of ILs used in industry.[57,58] EDLCs, or supercapacitors, are promising devices having high power density and energy density. What provides them with high capacitance is electric double layer formed at electrode surface, and it completely screens at sub-nanometer length scale the electric potential applied by the electrodes. The electric double layer being crucial for an EDLC's high capacitance, ILs are used as ionic species in electrolyte. Because their high viscosity makes them electrically less conductive, ILs mixed with acetonitrile, a conventional organic electrolyte, have been used in order to improve the electric conductivity.

Electrodes also determine properties of EDLCs as well as electrolyte. Graphene has many advantages as electrodes, and has been studied intensively, recently. Reduced graphene oxide (GO), however, has not been studied in simulation studies of EDLCs while it has been taken into account in recent experiment studies since it is very likely to have oxygen impurity in the process of reducing graphene oxide to make pristine graphene. We firstly reported the computational study on the interfaces between GO and liquid by varying the configuration on the GO electrodes,[57] where the electrode oxidation is controlled by the concentration of hydroxyl groups (-OH) on the GO surface.

Experimental debate on the relation between oxidation of graphene and capacitance of the EDLC prompted our study. Some studies have shown that oxidation enhances capacitance[59,60] while others suggest that graphene oxide have lower capacitance than pure graphene.[61–67] We found in our latest simulation study,[57] where we used pure ionic liquid electrolyte, $EMI^{+}BF_4{}^{-}$, that capacitance decreases with increasing oxidation in the electrode, which were ascribed to two factors: hindered reorganization ability of ions and widened electric double layer by hydroxyl groups in the electrode. The purpose of this present study is to find the relation between the oxide impurity in GO and the electrostatic properties of EDLCs, and to uncover the charging mechanism underneath it by comparing pure IL electrolyte and its mixture with acetonitrile.

Part I

Dynamic Heterogeneity of Model Ionic Liquids

Chapter 2

Introduction

Most ILs consist of bulky, asymmetric cations and small, symmetric anions. It has been reported that IL is much more viscous than its counterpart of neutral binary mixture,[13,68] and it becomes less viscous as the charge is distributed more homogeneously on the molecule, mostly on a cation,[6,69–71] leading us to expect that Coulomb interaction may influence their glassy dynamics, and that the charge distribution of an ionic component can significantly affect dynamic properties of the IL. According to experimental[68,72,73] and simulation[6–19,74–76] studies, ILs exhibit slow dynamical behavior that are typically characterized by subdiffusivity and nonexponential relaxation as in glass forming liquids.

The overall nonexponential dynamics in glass forming liquids may be ascribed to either homogeneously nonexponential relaxation behavior or the superposition of exponential relaxations with different relaxation times in two limiting cases. Extensive studies performed so far point toward the picture that the latter, heterogeneous dynamics, is the case with ILs,[6–19] which is in accordance with previous studies on other glass forming liq-

uids,[5] such as supercooled liquids,[20–47] polymer melts,[48–53] and colloids.[54–56] Time and length scale of dynamic heterogeneity is important for obtaining microscopic understanding of dynamical behavior of liquids, and they have been subject to intensive investigations, recently, in supercooled liquids[20–41] and polymer melts,[50–53] but very few in ILs.[19] The dynamic length scale adapted from the framework of conventional critical phenomena has been widely used in studies on dynamic heterogeneity.[5,19–25,35–37] The importance of time scale of dynamic heterogeneity in glassy dynamics and in glass transition also has been shown in both numerical and experimental research mainly from its phenomenological approach.[24–34,50–53] Despite such interest, the dynamic length and time scales of ILs and the relation between them have not been thoroughly understood.

Coarse-graining ILs is a very common strategy in reducing the computation time because performing simulations for ILs is very time-demanding due to not only their intrinsically slow dynamics but also Ewald summation method, which is inevitable for calculating long range interactions. In an effort to make the simulations of ILs efficient, various levels of coarse-grained models have been developed for studying their structural and dynamic properties.[6,8–10,13,14,77] Since our purpose of this study is to characterize the qualitative behavior of dynamic heterogeneity and to find the origin of it in ILs in molecular level, a simplest possible model maintaining glassy dynamics is the most suitable for this study.

For that purpose, we utilize two different, simple models of ILs introduced by a previous study.[6] One model mimics the case of symmetrical charge distribution in cation molecules, while the other asymmetric one in cations. In both models, asymmetry in the cation shape is introduced to pre-

vent the ILs from crystallizing. We also explore the neutral model with the same molecular shape. With these models, we study the dynamic properties of IL systems via performing molecular dynamics simulations. In particular, we focus on the issue of the correlation between the local charge distribution of cations and the dynamic heterogeneity of ILs by investigating the lifetimes of dynamic heterogeneity by calculating their three-time correlation functions (3TCFs) in these systems.

The validity of the 3TCF as a quantity measuring the dynamic heterogeneity is examined from the relation between the time scale of the 3TCFs and that of the two-point correlation functions, such as the structural relaxation and the relaxation of rotational motion. Moreover, the dependence of the dynamic heterogeneity time scale on the length scale of the structural relaxation time is explored. We find that the lifetime of the 3TCFs is the distinct time scale of dynamic heterogeneity, and we believe that this work is the first that has investigated the relation between the time scale of dynamic heterogeneity and the length scale of the structural relaxation in ILs.

The remainder of Part I is organized as follows. In Chapter 3 theoretical background of dynamic heterogeneity is briefly reviewed. Chapter 4 is devoted to model descriptions and simulation methods. In Chapter 5, we present our main results on the lifetime of dynamic heterogeneity in the model IL systems, and discuss our findings. Finally, we summarize the results and conclude in Chapter 6.

Chapter 3

Theoretical background of dynamic heterogeneity

We first briefly review the dynamic heterogeneity in the frame work of the four-point correlation functions, and in the breakdown of Stokes-Einstein relation. The former relates the dynamic heterogeneity directly relate to the glass transition by obtaining dynamic length scale that grows with temperature decreasing. In the latter the two time scales corresponding to diffusion and structural relaxation, respectively, are decoupled, and the dynamical heterogeneity induces the two dynamical processes decoupled. The two phenomena have not yet been found to rule out each other.

3.1 Four-point correlation functions

The formalism of four-point correlation functions has been widely studied as a frame work of dynamic heterogeneity.[5,20–23,37,41] A four-point density

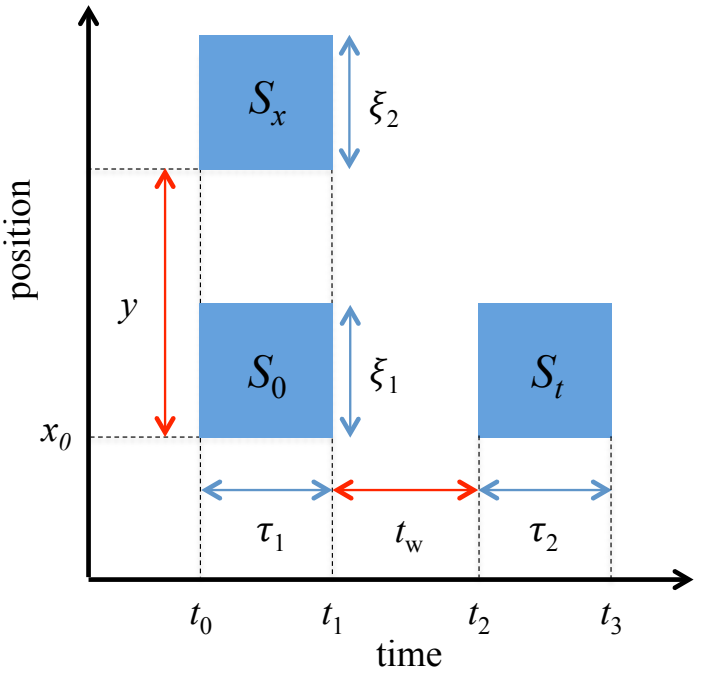

Figure 3.1: Overview of four-point correlation functions. G_4 correlates S_0 and S_x, and F_4 does S_0 and S_t. $\tau_1 = t_1 - t_0$, $t_w = t_2 - t_1$, and $\tau_2 = t_3 - t_2$.

correlation function,

$$G_4(y,t) = [\langle \rho(\mathbf{x}_0,t_0)\rho(\mathbf{x}_0,t_0+t)\rho(\mathbf{x}_0+\mathbf{y},t_0)\rho(\mathbf{x}_0+\mathbf{y},t_0+t)\rangle - \langle \rho(\mathbf{x}_0,t_0)\rho(\mathbf{x}_0,t_0+t)\rangle^2], \tag{3.1}$$

detects the correlation between the dynamics at the different positions x_0 and $x_0 + y$, where $\langle\cdots\rangle$ and $[\cdots]$ respectively denote average over the reference time t_0 and the reference space-point $\mathbf{x}_0$, and $\rho(\mathbf{x}', t')$ is the micro-

scopic density at position $\mathbf{x}'$ and time t'. Since this correlation function was originally coined for spin glass systems,[5,78] in order for Eq. (3.1) to be applicable in a continuous position space correlation between $\rho(\mathbf{x}_0, t_0)$ and $\rho(\mathbf{x}_0, t_0 + t)$ is coarse-grained in position space with ξ_1: $\rho(\mathbf{x}_0 + \mathbf{y}, t_0)$ and $\rho(\mathbf{x}_0 + \mathbf{y}, t_0 + t)$ with ξ_2.[5,23] Eq. (3.1), thus, becomes

$$\widetilde{G}_4(y, t; \xi_1, \xi_2) = [\langle \rho(\mathbf{x}_0, t_0)\rho(\mathbf{x}_0 + \mathbf{y}, t_0)\rho(\mathbf{x}_0 + \xi_1, t_1)\rho(\mathbf{x}_0 + \xi_2 + \mathbf{y}, t_1)\rangle - \langle \rho(\mathbf{x}_0, t_0)\rho(\mathbf{x}_0 + \xi_1, t_1)\rangle \langle \rho(\mathbf{x}_0, t_0)\rho(\mathbf{x}_0 + \xi_2, t_1)\rangle], \quad (3.2)$$

and it correlates the dynamics of S_0 and S_x delineated in Figure 3.1 with $t_1 - t_0 = \tau_1 = t$. The characteristic length scale of dynamic heterogeneity, ξ_{dh}, is obtained by varying y with the parameters usually fixed at $\tau_1 = \tau_\alpha$, $\xi_1 = \xi_2 = 2\pi/k$.[23] The time scale of the four-point correlation function is extracted from the four-point dynamic susceptibility, $\chi_4(k, t)$, which is the dynamic correlation between two regions integrated over all space of $\mathbf{y}$. Its explicit form, When $\widetilde{G}_4(y, t; \xi_1, \xi_2)$ is Fourier transformed in $\xi_1 = \xi_2 = 2\pi/k$ and y to become $S_4(q, t; k)$, and then a four-point dynamic susceptibility is defined: $\chi_4(k, t) = S_4(q = 0, t; k)$. $\chi_4(k, t)$ is the dynamic correlation between two regions integrated over all position space of y, a four-point dynamic susceptibility, $\chi_4(k, t) = \int d\mathbf{y}\widetilde{G}_4(\mathbf{y}, t)$, is obtained.

$$\chi_4(k, t) = N\Big[\Big\langle \hat{F}_s(\mathbf{k}, t_0, t_0 + t)^2 \Big\rangle - \Big\langle \hat{F}_s(\mathbf{k}, t_0, t_0 + t) \Big\rangle^2\Big], \quad (3.3)$$

depicts the dynamic fluctuation of the two-point correlator, $\hat{F}_s(\mathbf{k}, t_0, t_0 + t)$. The characteristic time scale, t_4, of dynamic heterogeneity in this frame work is defined as the time at which the dynamic fluctuation is the maximum. It has been reported, however, to be proportional and similar to the

time scale, τ_α, of a two-point density correlation function, *i.e.*, $t_4 \propto \tau_\alpha$,[40,41] and the models studied in this dissertation are no exceptions.

On the other hand, a three-time correlation function (3TCF) defined analogously to Eq. (3.2) yields a time scale distinct from t_4. The dynamical correlation between different time windows is expressed as[25–28,32,33,53]

$$\begin{aligned}\widetilde{F}_4(\tau_1, t_\mathrm{w}, \tau_2; \mathbf{k}_1, \mathbf{k}_2) = & \langle \hat{\rho}(-\mathbf{k}_1, t_0)\hat{\rho}(\mathbf{k}_1, t_1)\hat{\rho}(-\mathbf{k}_2, t_2)\hat{\rho}(\mathbf{k}_2, t_3)\rangle \\ & - \langle \hat{\rho}(-\mathbf{k}_1, t_0)\hat{\rho}(\mathbf{k}_1, t_1)\rangle \langle \hat{\rho}(-\mathbf{k}_2, t_2)\hat{\rho}(\mathbf{k}_2, t_3)\rangle \\ = & \left\langle \hat{F}_s(\mathbf{k}_1, t_0, t_1)\hat{F}_s(\mathbf{k}_2, t_2, t_3)\right\rangle \\ & - \left\langle \hat{F}_s(\mathbf{k}_1, t_0, t_1)\right\rangle \left\langle \hat{F}_s(\mathbf{k}_2, t_2, t_3)\right\rangle, \end{aligned} \tag{3.4}$$

where the two-point correlator, $\hat{F}_s(\mathbf{k}, t', t'')$, correlates between $\hat{\rho}(-\mathbf{k}, t')$ and $\hat{\rho}(\mathbf{k}, t'')$ in Eq. (3.4). By adopting $\hat{F}_s(\mathbf{k}, t', t'') = \frac{1}{N}\sum_j \cos[\mathbf{k}\cdot\Delta\mathbf{r}_j(t', t'')]$ as in Eq. (5.3) and fixing the length scale, $\mathbf{k}_1 = \mathbf{k}_2 = \mathbf{q}$, the first term of Eq. (3.4) becomes

$$\begin{aligned}&\left\langle \frac{1}{N}\sum_{j=1}^{N} \cos\left[\mathbf{q}\cdot\Delta\mathbf{r}_j(t_0, t_0+\tau_1)\right]\right. \\ &\left.\times \frac{1}{N}\sum_{l=1}^{N} \cos\left[\mathbf{q}\cdot\Delta\mathbf{r}_l(t_0+\tau_1+t_\mathrm{w}, t_0+\tau_1+t_\mathrm{w}+\tau_2)\right]\right\rangle. \end{aligned} \tag{3.5}$$

For brevity of this argument we will consider the self part of Eq. (3.5), *i.e.*, $j = l$ of the summations. We thus define the 3TCF as[24,25,28,32,33,53]

$$\begin{aligned}F_4(\tau_1, t_\mathrm{w}, \tau_2; q) = \left\langle \frac{1}{N}\sum_{j=1}^{N} \left\{ \cos\left[\mathbf{q}\cdot\Delta\mathbf{r}_j(t_0, t_0+\tau_1)\right]\right.\right. \\ \left.\left. \times \cos\left[\mathbf{q}\cdot\Delta\mathbf{r}_j(t_0+\tau_1+t_\mathrm{w}, t_0+\tau_1+t_\mathrm{w}+\tau_2)\right]\right\}\right\rangle, \end{aligned} \tag{3.6}$$

which correlates the dynamics between the two time intervals, $(t_0, t_0+\tau_1)$ and $(t_0+\tau_1+t_\mathrm{w}, t_0+\tau_1+t_\mathrm{w}+\tau_2)$, or the dynamics of S_0 and S_t in Figure 3.1. The rotational form of the 3TCF is defined straightforward by substituting $P_l(\hat{\mathbf{u}}_j(t'')\cdot\hat{\mathbf{u}}_j(t'))$ for $\cos[\mathbf{q}\cdot\Delta\mathbf{r}_j(t',t'')]$ in Eq. (3.6). While G_4 detects heterogeneous dynamics in different positions, thus is able to extract the length scale of dynamic heterogeneity, F_4 does in different times, thus, the time scale of dynamic heterogeneity. Although F_4 is defined analogously to G_4, it can be understood intuitively.

When the waiting time becomes greater, $t_\mathrm{w}\to\infty$, the dynamics of the two time intervals are uncorrelated that $F_4(\tau_1, t_\mathrm{w}, \tau_2; q)$ converges to $F_\mathrm{s}(q,\tau_1)F_\mathrm{s}(q,\tau_2)$, where a physical meaning of Eq. (3.6) can be derived. Given a dynamic fluctuation of particle j in a certain time duration τ_1, with the 3TCF we can figure out how long it must wait for the memory of this fluctuation to be lost. Here, the first part of Eq. (3.6) acts as a dynamic filter.[52] For faster particles $\cos[\mathbf{q}\cdot\Delta\mathbf{r}_j(t_0, t_0+\tau_1)]$, the first part of $F_4(\tau_1, t_\mathrm{w}, \tau_2; q)$, has smaller values, but for very slow particles the cosine value is close to one. Slower particles have more contribution on $F_4(\tau_1, t_\mathrm{w}, \tau_2; q)$, so the dynamic filter selects subpopulations of particles moving slower.

After dynamically filtering slow particles, we quantify how fast the subpopulations recover to the average dynamics. The time scale of dynamic heterogeneity is the lifetime of the correlation function,[25,33]

$$\Delta F_4(t_\mathrm{w}; q, \tau_1, \tau_2) = \frac{F_4(\tau_1, t_\mathrm{w}, \tau_2; q) - F_\mathrm{s}(q,\tau_1)F_\mathrm{s}(q,\tau_2)}{F_4(\tau_1, 0, \tau_2; q) - F_\mathrm{s}(q,\tau_1)F_\mathrm{s}(q,\tau_2)}, \tag{3.7}$$

and from this we can focus on the dependence of dynamic heterogeneity on t_w. The value of $\Delta F_4(t_\mathrm{w})$ indicates how much dynamically heterogeneous the system is, and the time scale at which the $\Delta F_4(t_\mathrm{w})$ goes to zero is that

of dynamic heterogeneity.

The waiting time is an important variable to quantify the correlation between the dynamics at the two time intervals. It is required to fix some of the parameters, q, τ_1, and τ_2 before studying the dependence of the 3TCF on the waiting time. It is obvious to set $\tau_1 = \tau_2 = \tau_\alpha$ since the dynamic heterogeneity is observed to be more prominent at time scale close to $\tau_\alpha \approx t_4$. We, then, fix the length scale with 4 different q values indicated in Figure 5.8 from q^* to $q_0/2$. The lifetime of ΔF_4, $\tau_{\rm dh}(q)$, is defined such that $\Delta F_4(t_{\rm w} = \tau_{\rm dh}; q, \tau_\alpha, \tau_\alpha) = e^{-1}$, and its rotational form is $\tau_{\rm dh,R}$.

3.2 Dynamic heterogeneity and the Stokes-Einstein relation breakdown

The Stokes-Einstein (SE) relation, $D \sim k_{\rm B}T/\eta$, where η is shear viscosity, is valid in wide range of liquids, but it breaks down in glass forming liquids near glass transition temperature, and it has been adopted as an evidence showing glassy dynamics. Two alternate relations have been adopted in studies on the violation of the SE relation in order to reduce computation time requiring for calculating the shear viscosity. In one group of studies τ is used as the approximation for η, $D\tau/T$ thus becomes constant.[79,80] In the others η is approximated to be τ/T to make $D\tau$ constant.[8,42,47] Following the latter way we look for the breakdown of the SE and the Debye-Stokes-Einstein (DSE) relations. When the dynamics of the system is well described by mean-field behavior, $F_{\rm s}(q,t) = \exp[-q^2 Dt]$ and $C_l(t) = \exp[-l(l+1)D_{\rm R}t]$, thus $q^2 D\tau_\alpha = 1$ and $l(l+1)D_{\rm R}\tau_{\rm R}^{(l)} = 1$.

The breakdown of the SE relation has been investigated intensively in

kinetically constrained models (KCMs),[8,34,35,42,47] which is basically similar to the lattice gas model. The uniqueness of the models is that the interaction between the defects is not included in its Hamiltonian, but is included through kinetic constraints. The two time scales, the persistence time and the exchange time, represent two dynamic processes, the structural relaxation and the diffusion, respectively. The persistence time, τ_{p}, is defined as the waiting time for a particle to encounter its first excitation, and the exchange time, τ_{x}, is defined as the time interval between successive excitation events. In a stochastic process, the distributions of the two times are identical with Poisson distribution. When temperature cools down, the two processes become decoupled, and it describes the decoupling between diffusion and structural relaxation. In this context, it has been received that the breakdown of the SE relation is related to the dynamic heterogeneity.[8,34,35,42,47]

Chapter 4

Models and simulation methods

We will firstly introduce toy models of ionic liquids and a neutral model by removing the charges from the IL models, and describe detail information of them. In order to compare our main results, the SE relation and the lifetime of dynamic heterogeneity, to other well-known models, for supercooled liquids which have been studied intensively for glassy dynamics. Only a brief information of the well-known models, except the models in Section 4.1, is included in the corresponding sections, Sections 4.2.1 to 4.2.3, because the detailed description of the models can be found in the references therein.

4.1 Toy models of ionic liquids and their neutral counter part

Most ILs consist of bulky, asymmetric cations and small, symmetric anions. Preferred choices for cations include 1-alkyl-3-methylimidazolium, pyridinium, pyrrolidinium, tetraalkylammonium, and tetraalkylphosphonium ions, and for anions tetrafluoroborate (BF_4), hexafluorophosphate (PF_6), trifluoromethane-

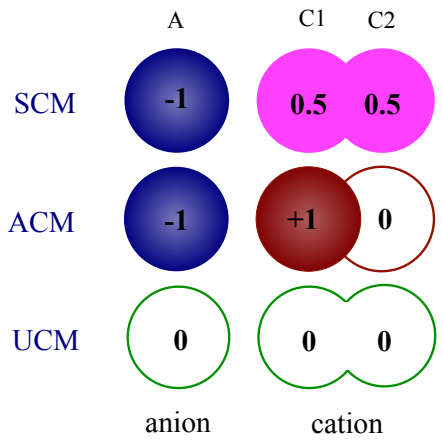

Figure 4.1: Schematic representation of the three models: the symmetric-charge model, or SCM (top) and the asymmetric-charge model, or ACM (middle) representing ILs, and the uncharged model, or UCM (bottom) of uncharged glass forming liquids with the same molecular structure. In SCM two spherical cationic components share the positive charge equally for each having 0.5 e, and in ACM only one sphere (C1) has the positive charge, 1.0 e. Their uncharged counterpart UCM, however, does not have any charged components.

sulfonate, and bis(trifluoromethylsulfonyl)imide ions. Although it is not possible that the ions take different charge distribution with the molecular geometry fixed in real experiments, it has been reported that the liquid becomes less viscous as the charge is distributed more homogeneously on the molecule from simulation studies,[6,70,71] where it is expected that the

charge distribution of an ionic component can significantly affect dynamic properties of the ILs. We thus choose two extreme cases of charge distribution: symmetric and asymmetric.

Our key purpose is to focus on the effect of charge distributions of IL molecules on their dynamic properties and find their qualitative trends, or scaling relations, rather than to reproduce quantitatively exact values of real systems. We are exempted from realizing molecular details, and in order to make the simulation efficient we employ two simple, coarse-grained models of ILs that were previously introduced in Ref. 6 and an uncharged model as a counterpart of the two IL models. Their schematic molecular structures are shown in Figure 4.1. Because the molecular details are simplified by coarse-graining, including charge fluctuation in the molecules is not a clever tactics, we fix the partial charges neglecting the polarization effect. We choose a two-site model for the cation since it mimics an IL system better than a single-site cation model, and it simplifies more than preexisting three-site and four-site coarse-grained models.[8,13,14] Less symmetric molecular structure of this model not only prevents the crystallization that would occur more easily in a single-site model, but it also enables us to investigate rotational dynamics, thus we can investigate translational and rotational glassy dynamics with this model. Its simplicity relative to other coarse-grained models enables us to simulate for a longer time.

In both models of ILs, the anion is represented by a single spherical particle (A) of mass, m, 200 amu, and the cation by two spherical particles (C1 and C2) connected through a rigid bond, where the mass of each particle is set to be 100 amu so that the total mass of cation is the same as that of anion. In the symmetrically charged model (SCM) the two spheres have

the same charges (+0.5 e, where e is the elementary charge), while in the asymmetric-charge model (ACM) one (C1) of the two spherical particles has +1.0 e and the other (C2) zero. The anion has −1.0 e for both models. The uncharged model (UCM) has the same molecular structure as the IL models except that all the components do not have charges, but we stick to "cation" and "anion" for big and small species of UCM for the sake of convenience. On top of the Coulomb interactions between charged particles, they also interact with Lennard-Jones potential with each other in all models. We could find no crystallization within the simulation times at each temperature, except that ACM crystallizes at $T = 1.73$, right below the lowest temperature studied for ACM.

We perform classical molecular dynamics (MD) simulation using the above models. All the MD trajectories are obtained from GROMACS 4.5 MD package program.[81] The total potential energy is given by the sum of the pairwise interactions of two different types: the repulsive Lennard-Jones (LJ) potential and the Coulomb potential,

$$U_{\text{total}} = \sum_{<i,j>} \left\{ U_{\text{LJ}}(r_{ij}) + U_{\text{Coulomb}}(r_{ij}) \right\}, \tag{4.1}$$

where $< i, j >$ indicates that the sum is performed over the i-th and j-th coarse-grained particles, and

$$U_{\text{LJ}}(r_{ij}) = 4\epsilon_{ij} \left[\left(\frac{\sigma_{ij}}{r_{ij}} \right)^{12} - \left(\frac{\sigma_{ij}}{r_{ij}} \right)^{6} + \frac{1}{4} \right] H(r_{\text{cut}} - r_{ij}) \tag{4.2}$$

and

$$U_{\text{Coulomb}}(r_{ij}) = \frac{1}{4\pi\epsilon_0} \frac{q_i q_j e^2}{r_{ij}}. \tag{4.3}$$

Here, $H(r_{\rm cut}-r_{ij})$ is the Heaviside step function, where the cutoff distance is set to be $r_{\rm cut} = 2^{1/6}\sigma_{ij}$ in order to make the Lennard-Jones potential purely repulsive by adopting the Weeks-Chandler-Andersen (WCA) potential.[82] In all the models $\epsilon_{ij} = \epsilon = 2$ kJ/mol and $\sigma_{ij} = \sigma = 0.5$ nm for all i, j-pairs, and the bond between the two spheres is rigid with a bond distance $d = 0.8\sigma$. q_i is the partial charge of i species (Figure 4.1). With the unit length, energy, and mass, σ, ϵ, and m, respectively, the other units are converted by the following relations: unit time, $t_0 = (m\sigma^2/\epsilon)^{1/2} = 5$ ps, unit temperature, $T_0 = \epsilon/k_{\rm B} = 240.5$ K, unit charge, $q_0 = (4\pi\epsilon_0\sigma\epsilon)^{1/2} = 0.08484\ e$, and unit pressure, $P_0 = 262.2$ atm.

The model parameters used in this study are comparable to ones from previous simulation studies on ILs, ranging from EMIM to BMIM for the cation and tetrafluoroborate (BF_4) or PF_6 for the anion.[8,13,76,83] With those parameters SCM remains as liquid state at room temperature. As the purpose of this study is focused on finding out general properties of ILs with respect to the charge distribution on the molecules, these simple models with plausible parameters are thought to be good enough model systems to investigate dynamic properties.

All simulations are performed at the fixed reduced density $\rho^* = \rho\sigma^3 = 0.716$, where $\rho = (N_+ + N_-)/V$ is the total number density with N_+ and N_- being the number of cations and anions, respectively. In our simulations we use a total of 4096 ions, *i.e.*, 2048 pairs of IL molecules in our simulations, $N_{\rm pair} = N_+ = N_- = 2048$ contained in the cubic simulation box of a linear dimension of $L = 17.88$, and a periodic boundary condition is applied. The box size is determined by equilibrating with NPT simulation at $P = 10$ and $T = 1$, for SCM, and we fix all the simulation boxes of all models at

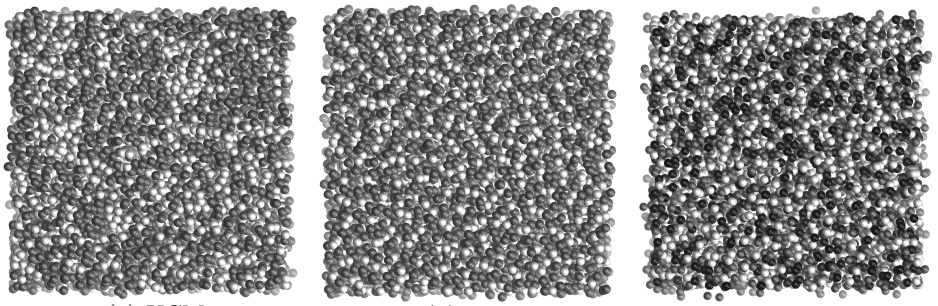

(a) UCM (b) SCM (c) ACM

Figure 4.2: Snapshots of UCM (a), SCM (b), and ACM (c) at the lowest temperature of each model. Dark (gray or black) and white particles respectively denote cations and anions. For ACM we distinguish the uncharged (0 e) component from the charged (+1.0 e) one with black and gray. Compared to UCM, IL models show alternating structure preventing the same species from being positioned at the nearest neighbor.

all temperatures with this value. Even if the systems are in high pressure condition and have different pressures by fixing the volume with the same value, the qualitative trends of dynamics should be little affected.[84] We also checked our results with different size of systems such as $N_{\text{pair}} = 512$, 1024, 2048, and 4096 to find no significant finite size effect with $N_{\text{pair}} = 2048$ on the structural relaxation times. We employ the NVT ensemble combined with the Nosé-Hoover thermostat in our simulations. The time step is chosen as $\delta t = 0.0004$, and the relaxation time constant for the thermostat as $200\delta t$. Both the LJ potential and the Coulomb potential are truncated at 5. For calculating long-range electrostatic interaction PME is used. The Verlet leapfrog algorithm is employed to integrate the equations of

motion. Each system is first equilibrated from a higher temperature until the energy fluctuation is found to be stable for around its structural relaxation time, τ_α, and then a production run is carried out from this equilibrated configuration to obtain a sample trajectory, whose total run time is about 40 times of the τ_α at each temperature. At all temperatures studied in this work, 10 independent trajectories are produced, and structural and dynamic properties are averaged over those trajectories.

4.2 Models of glass-forming binary mixtures

4.2.1 Kob-Andersen model

The Kob-Andersen (KA) model is a mixture of two species, A and B, and the ratio of the numbers of two particles, $N_\mathrm{A} : N_\mathrm{B} = 8 : 2$.[85] The interactions between the particles are purely the Lennard-Jones potential given by

$$U_\mathrm{LJ}(r_{ij}) = 4\epsilon_{ij}\left[\left(\frac{\sigma_{ij}}{r_{ij}}\right)^{12} - \left(\frac{\sigma_{ij}}{r_{ij}}\right)^{6} + \frac{1}{4}\right], \tag{4.4}$$

where the relations of the energy and the size parameters between each species are $\epsilon_\mathrm{BB} = 0.5\epsilon_\mathrm{AA}$, $\epsilon_\mathrm{AB} = 1.5\epsilon_\mathrm{AA}$, and $\sigma_\mathrm{BB} = 0.88\sigma_\mathrm{AA}$, $\sigma_\mathrm{AB} = 0.8\sigma_\mathrm{AA}$, respectively. The interaction is cut off at $r = 2.5\sigma_\mathrm{ij}$. The two species have the same masses: $m_\mathrm{A} = m_\mathrm{B}$. The reduced units for length, temperature, and time are σ_AA, $\epsilon_\mathrm{AA}/k_\mathrm{B}$, and $\sqrt{m_\mathrm{A}\sigma_\mathrm{AA}^2/\epsilon_\mathrm{AA}}$. The integration time step is set to $\delta t = 0.001$, and the total number density is fixed with $\rho = 1.2$ with $N_\mathrm{A} = 4000$ and $N_\mathrm{B} = 1000$. The temperatures are scanned over $T =$ 5, 2, 1, 0.7, 0.6, 0.55, 0.5, 0.47, 0.45, 0.44, 0.43, and 0.42.

4.2.2 Wahnström model

The Wahnström model has the ratio, $N_{\mathrm{A}} : N_{\mathrm{B}} = 5 : 5$.[86] The interactions between the particles are the same as Section 4.2.1, with the relations of the parameters, $\epsilon_{\mathrm{BB}} = \epsilon_{\mathrm{AA}}$, $\sigma_{\mathrm{AA}} = 1.2\sigma_{\mathrm{BB}}$, and $m_{\mathrm{A}} = 2m_{\mathrm{B}}$. The interaction is cut off at $r = 2.5\sigma_{\mathrm{ij}}$. The relation between different species satisfies the Lorentz-Berthelot rules, $\sigma_{AB} = (\sigma_{\mathrm{AA}} + \sigma_{\mathrm{BB}})/2$ and $\epsilon_{\mathrm{AB}} = \sqrt{\epsilon_{\mathrm{AA}}\epsilon_{\mathrm{BB}}}$. The reduced units for length, temperature, and time are σ_{BB}, $\epsilon_{\mathrm{BB}}/k_{\mathrm{B}}$, and $\sqrt{m_{\mathrm{B}}\sigma_{\mathrm{BB}}^2/\epsilon_{\mathrm{BB}}}$. $\delta t = 0.001$, and $\rho = 0.75$ with $N_{\mathrm{A}} = 4000$ and $N_{\mathrm{B}} = 4000$. The temperatures are scanned over $T = 1$, 0.7, 0.63, and 0.58.

4.2.3 Wahnström model with WCA potential

The LJ potential in the Wahnström model is replaced with the WCA potential with other parameters fixed as in Section 4.2.2.[47] The temperatures are scanned over $T = 5$, 1, 0.5, 0.44, 0.4, 0.38, and 0.36.

Chapter 5

Results and discussion

5.1 Liquid structure

The structure of the models is firstly investigated by calculating the radial distribution functions (RDFs), $g(r)$, for all the models, where r is the distance between the centers of mass of the ions. While we have calculated RDFs at all the temperatures studied in this study, those at the highest ($T = 6$ for both IL models, and 1.14 for UCM) and the lowest ($T = 1.04$, 1.75, and 0.29 for SCM, ACM, and UCM, respectively) temperatures are shown in Figure 5.1. g_{CC}, g_{AA}, and g_{CA} are the RDFs of cation-cation, anion-anion, and cation-anion pairs, respectively. Both IL models have similar liquid structures at high temperature (left panels of Figure 5.1).

Firstly, we note that all the models exhibit typical structures of amorphous liquid, and they do not show any sign of crystallizations at all temperatures we have studied. The first peak of RDF determines the closest length scale, which is 1 for all the species in UCM, the same as the value of σ of our models. In the ILs' RDFs the first peaks between the equally

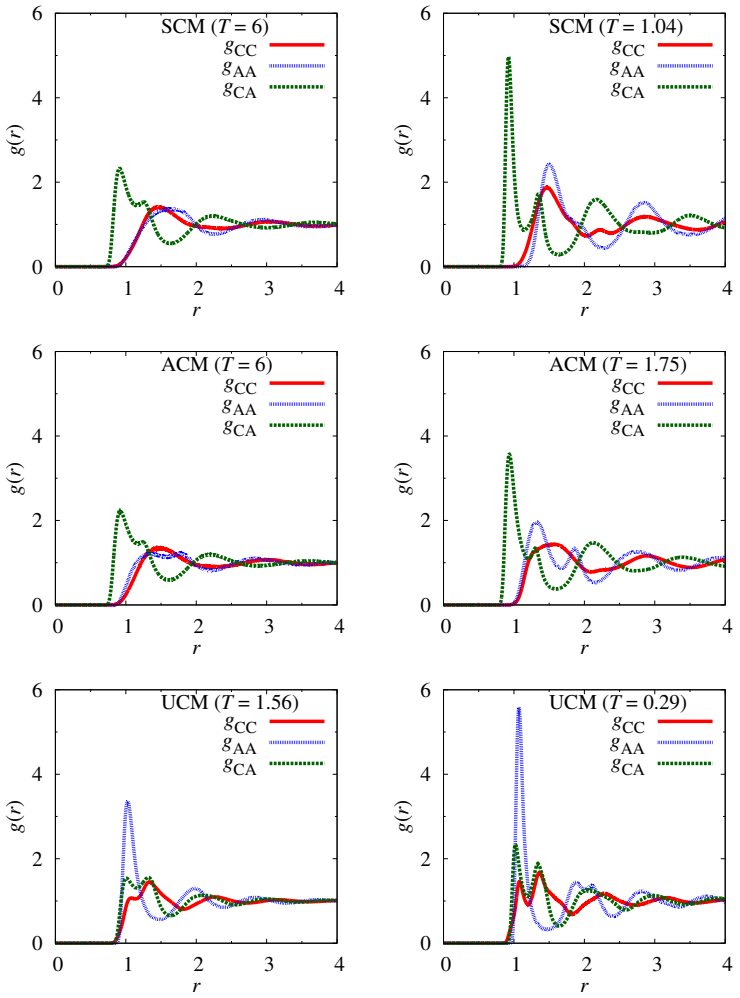

Figure 5.1: Center of mass radial distribution functions, RDFs, at the highest temperatures (left) and the lowest temperatures (right) of SCM (top), ACM (middle), and UCM (bottom), respectively.

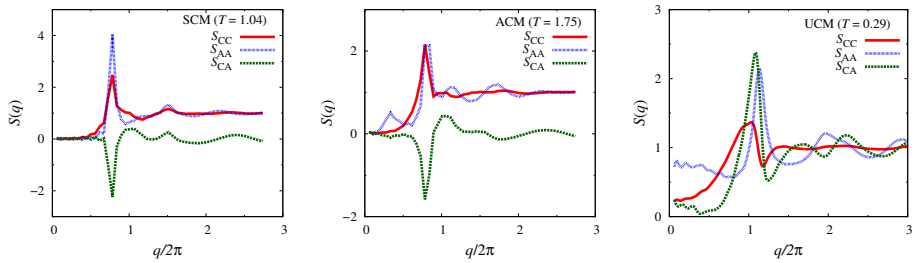

Figure 5.2: The static structure factors, $S(q)$, are obtained by integrating $g(r)$ (Eq. (5.1)), and although it may not have high statistical quality, the position of the peaks are quite robust.

charged species ($\sigma_+ = 1.46$ and $\sigma_- = 1.5$ for SCM, and 1.54 and 1.32 for ACM) appear at a distance longer than σ due to the repulsive interactions while those between the oppositely charged species ($\sigma_\pm = 0.92$ and 0.94 for SCM and ACM, respectively) at a distance shorter than σ due to attractive interactions. The difference between $\sigma_\pm$ and σ_+ or σ_- is consistent to the alternating structure of the IL models found in Figure 4.2.

The static structure factor, $S(q)$, is obtained from Fourier transform of the $g(r)$,

$$S_{\alpha\beta}(q) = (1 - \delta_{\alpha\beta}) + 4\pi \int_0^\infty r \frac{\sin qr}{q} \{g_{\alpha\beta}(r) - 1\} dr, \tag{5.1}$$

where α and β are indices for ion species, cation or anion (see Figure 5.2). In all pairs, except for cross pairs in IL models, the first peak, $q_{\max}^{(\alpha\beta)}$ of $S_{\alpha\beta}(q)$ are consistent to the first peak, $r_{\max}^{(\alpha\beta)}$, of $g_{\alpha\beta}(r)$. In IL models , however, $q_{\max}^{(CA)}$ does not fall into $r_{\max}$ but rather close to $2\pi/r_{\max}^{(CC)}$ or $2\pi/r_{\max}^{(AA)}$. $g_{\mathrm{CA}}(r)$ is approximately shifted by -0.5 from g_{CC} or g_{AA}, and this shift causes the phase change of $S(q)$ since the first peak of $g(r)$ contributes the

most to the $S(q)$. In the equivalent equation, $S(q) = 1/N\langle\rho_k\rho_{-k}\rangle$, where $\rho_k = \sum_{<ij>} \cos \mathbf{q} \cdot \mathbf{r}_{ij}$, most contributions are from $r_{ij} \approx r_{\max}$. If the two length scales, $2\pi/q_{\max}$ and $r_{\max}$, coincide, $S(q_0)$ is positive. But in the case of C-A pair because $q_{\max} \approx 2\pi/1.5r_{\max}$, most contributions are negative, thus gives the negative peak of $S_{\mathrm{CA}}(q)$. Among the two different length scales we firstly choose $r_{\max}^{(CA)}$, and then $r_{\max}^{(CC)}$ and $r_{\max}^{(AA)}$, close to $2\pi/q_{\max}^{(CA)} > r_{\max}^{(CA)}$ for each species in order to investigate dynamic properties in the next section.

The shapes of the RDFs of both IL models are generally similar to each other. At the high temperature, $T = 6$, the structures of RDF are very similar in both cases while the maximum peak splits into two peaks in anion–anion RDF for ACM. For example, in the case of anion-anion RDF of ACM at $T = 1.75$, there is a distinct second peak located at $r \approx 1.8$ while it is weakened in SCM. Also, the cation-cation RDF appears more broader in ACM than in SCM. The fact that positive charges are distributed more asymmetrically in ACM than in SCM makes it possible for cations to have more local arrangements, which yields a broader first peak in ACM. The environments where a particle is positioned are different for both models. SCM provides less complex environment due to symmetry in the charge distribution of the cation despite the geometrical asymmetry while for ACM an anion forms a strong ion pair preferentially to one (C1) of the two cationic components, which is a feasible motive inducing structural heterogeneity, and this may affect dynamic properties. We will discuss this point later in this Part.

5.2 Dynamic properties

The self part of the van Hove correlation function,[87]

$$G_s(\mathbf{r}, t) = \left\langle \frac{1}{N} \sum_{j=1}^{N} \delta \left[\Delta \mathbf{r}_j(t_0, t_0 + t) - \mathbf{r} \right] \right\rangle, \tag{5.2}$$

is a distribution function for a particle moving a distance r for the time duration t, where $\Delta \mathbf{r}_j(t_0, t_0 + t) = \mathbf{r}_j(t_0 + t) - \mathbf{r}_j(t_0)$, $\mathbf{r}_j(t')$ is the position vector of the center of mass of the ion j at time t', and $\langle \cdots \rangle$ denotes average over the reference time t_0. Figure 5.3 shows the displacement distributions, $P(\log_{10}(\delta r); t) = 4\pi \ln 10 \delta r^3 G_s(\delta r, t)$ of a selected system.

A two-point correlation function characterizing structural relaxation is

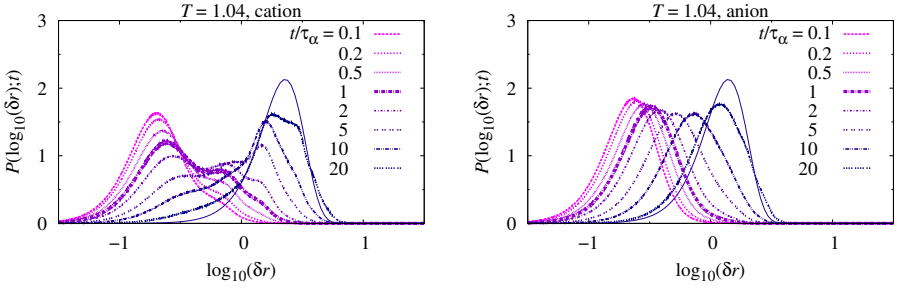

Figure 5.3: Time dependence of the displacement of SCM for the cation (left) and the anion (right) at $T = 1.04$. t increases from left to right. With the longer t, the van Hove function becomes the more similar to Gaussian, the solid line with the longest t.

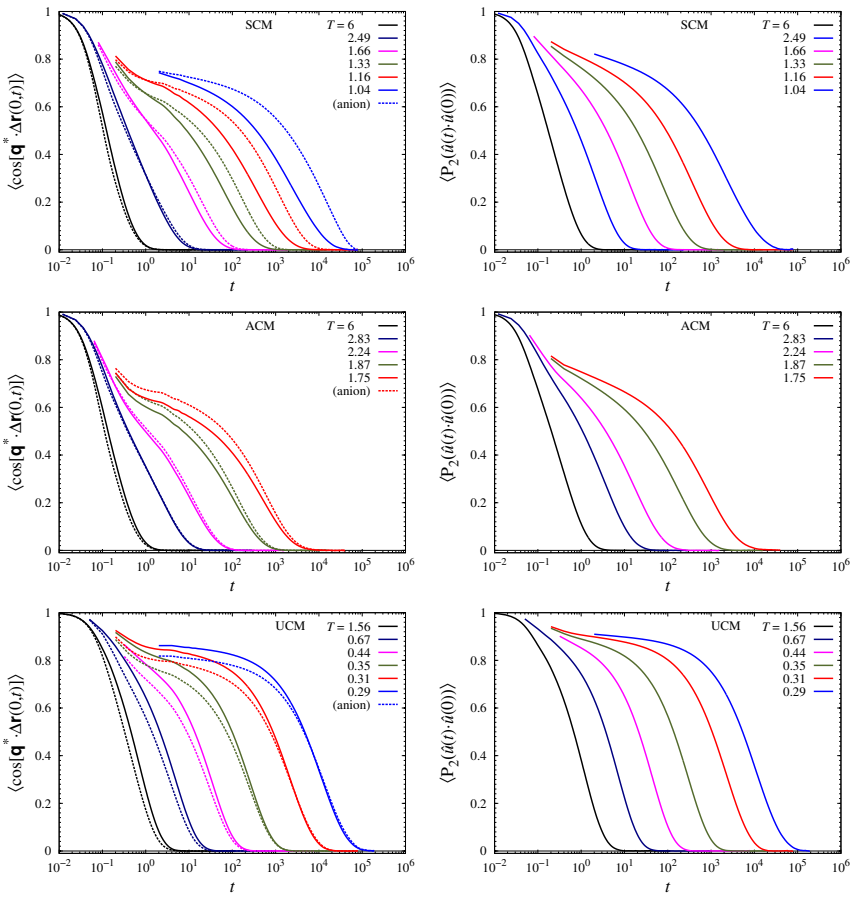

Figure 5.4: ISFs (left) at the selected temperatures (from left to right decreasing temperature) for the cation (full line) and the anion (dashed line) at the length scale, $q = q^* = 2\pi/\sigma_{\pm}$, where $\sigma_{\pm}$ is the peak position of g_{CA} (Figure 5.1) in SCM (top), ACM (middle), and UCM (bottom).

the self-intermediate scattering function (ISF),

$$F_{\rm s}(q,t) = \left\langle \frac{1}{N}\sum_{j=1}^{N} \exp\left[-i\mathbf{q}\cdot\Delta\mathbf{r}_j(t_0,t_0+t)\right] \right\rangle$$
$$= \left\langle \frac{1}{N}\sum_{j=1}^{N} \cos\left[\mathbf{q}\cdot\Delta\mathbf{r}_j(t_0,t_0+t)\right] \right\rangle, \qquad (5.3)$$

which is obtained by Fourier transform of $G_s(\mathbf{r},t)$. We take $q = q^* = |\mathbf{q}^*| = 2\pi/\sigma_{\pm}$, where $\sigma_{\pm}$ is the distance at the first peak of the radial distribution function, $g_{\rm CA}(r)$, of the cation-anion pair, and it is set to be the shortest length scale, the distance between the cation and the anion, $q^* = 6.83$, 6.68, and 6.28 for SCM, ACM, and UCM, respectively. We compare the time scales of $F_{\rm s}(q^*,t)$ and $F_{\rm s}(q_0,t)$, where the latter is more conventional.[8,44] q_0 for the cation and the anion respectively are the maximum positions of the static structure factors, $S_{\rm CC}(q)$ and $S_{\rm AA}(q)$, calculated by Fourier transform of $g_{\rm CC}(r)$ and $g_{\rm AA}(r)$, and the values are $q_0 = 4.83(4.83)$, 4.99(5.07), and 4.69(4.69) for cation(anion) of SCM, ACM, and UCM, respectively. We will compare the results with two more different q values: π and $q_0/2$. For the wave vector, $\mathbf{q}$, being isotropic, we calculate $F_{\rm s}(q,t)$ in terms of cosine as in Eq. (5.3) instead of exponential for dynamic filtering discussed later in section 5.3. The α-relaxation time, $\tau_\alpha(q)$, is defined such that $F_{\rm s}(q, t = \tau_\alpha) = 1/e$.

The rotational dynamics is also taken into account in order to find its relation to the translational dynamics. The correlation function characterizing rotational dynamics is defined as

$$C_l(t) = \left\langle \frac{1}{N}\sum_{j=1}^{N} P_l(\hat{\mathbf{u}}_j(t)\cdot\hat{\mathbf{u}}_j(0)) \right\rangle, \qquad (5.4)$$

where P_l is Legendre polynomial of order l, and $\hat{\mathbf{u}}_j(t')$ is the orientation vector of the j-th cation at time t'. The rotational relaxation time, $\tau_{\mathrm{R}}^{(l)}$, is defined such that $C_l(t = \tau_{\mathrm{R}}^{(l)}) = 1/e$, and we take $l = 2$ for its experimental significance.[46,54]

Comparing the length scales, q_0 and q^*, we find that with q^* the $F_{\mathrm{s}}(q,t)$ and $C_2(t)$ show the more similar decays, and the two time scales of the cation are comparable, $\tau_{\mathrm{R}}^{(2)} \approx \tau_\alpha(q^*)$, with the scaling relation, $\tau_{\mathrm{R}}^{(2)} \propto \tau_\alpha(q^*)$, shown in Figure 5.6. $F_{\mathrm{s}}(q^*,t)$ and $C_2(t)$ at the selected temperatures for the cation (full line) and the anion (dashed line) are shown in Figure 5.4. Both correlation functions at high temperatures show single decay while at low temperatures the process splits into two steps and the long time decay is nonexponential, and this nonexponentiality becomes greater as temperature decreases. According to experimental[29,30,50] and simulation studies[48,49] on glass forming liquids, this nonexponential decay of translational dynamics is attributed to heterogeneous dynamics.

τ_α of ACM increases more steeply than for SCM as temperature decreases (Figure 5.6). All the models show Arrhenius behavior at high temperature, and they start to show super-Arrhenius behavior at T <2.5, 3.6, and 0.6 for SCM, ACM, and UCM, respectively, $\tau \propto \exp[A/T^\nu]$, where $\nu > 1$, thus fragile. Two major fitting laws of the super-Arrhenius behavior of fragile liquids are VFT and parabolic[88,89] forms, which have different origin of fragility: whether there is finite temperature glass transition (the former) or there is no such transition (the latter). Both are fitted well (Figure 5.6), however, in the temperature range of our simulations. Since ACM is easy to crystallize below the lowest temperature in this work, the range is quite narrow. SCM and UCM are not thought to be in deeply supercooled

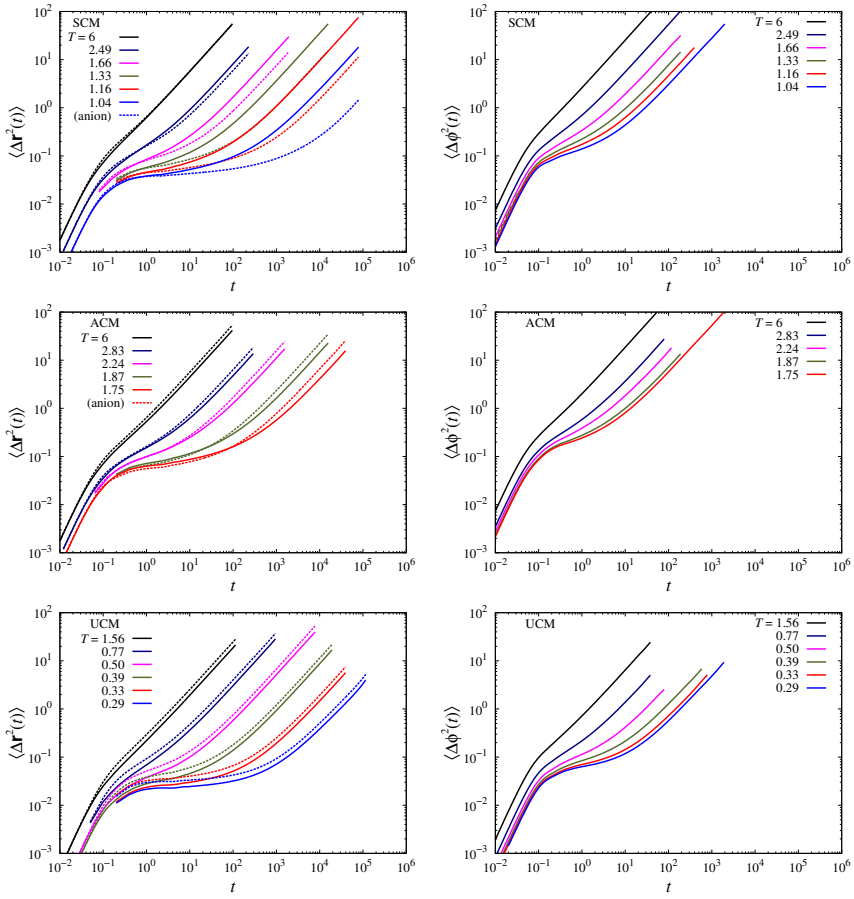

Figure 5.5: MSDs at the selected temperatures (from left to right decreasing temperature) of SCM (top), ACM (middle), and UCM (bottom), where the left panels indicate translational motion for the cation (full line) and the anion (dashed line), and the right ones rotational motion of the cation.

regime that in this temperature range we cannot discuss the validity of the two explanations. From its appearance perspective ACM seems the most fragile.

Another way of obtaining the dynamical properties is through the mean squared displacement (MSD) defined as

$$\left\langle \Delta \mathbf{r}^2(t) \right\rangle = \left\langle \frac{1}{N} \sum_{j=1}^{N} |\Delta \mathbf{r}_j(t_0, t_0 + t)|^2 \right\rangle, \tag{5.5}$$

and the mean squared angular displacement (MSAD) as

$$\left\langle \Delta \phi^2(t) \right\rangle = \left\langle \frac{1}{N} \sum_{j=1}^{N} |\Delta \phi_j(t_0, t_0 + t)|^2 \right\rangle, \tag{5.6}$$

where

$$\Delta \phi_j(t', t'') = \int_{t'}^{t''} dt \omega_j(t), \tag{5.7}$$

and $\omega_j(t)$ is the angular velocity of the j-th cation at time t.[43–45,56] The translational diffusion constant is obtained from the Einstein relation,[87] $D = \lim_{t\to\infty} \left\langle \Delta \mathbf{r}^2(t) \right\rangle / 6t$, and we fit the MSDs at the long time regime, *i.e.*, the time scale at which $\left\langle \Delta \mathbf{r}^2(t) \right\rangle \propto t$. The rotational diffusion constant, $D_{\mathrm{R}} = \lim_{t\to\infty} \left\langle \Delta \phi^2(t) \right\rangle / 4t$, is obtained from the MSADs. The MSDs for the cation and the anion and the MSADs for the cation are calculated for several temperatures ranging from $T = 1.04$ to 6 for SCM, $T = 1.75$ to 6 for ACM, and $T = 0.29$ to 1.56 for UCM as presented in Figure 5.5. At low temperature the time scales for all the systems can be separated into three distinct time regimes: the ballistic regime at short time ($\left\langle \Delta \mathbf{r}^2(t) \right\rangle \propto t^2$), the diffusive regime at long time ($\propto t$), and the subdiffusive regime at intermediate time ($\propto t^\alpha, 0 < \alpha < 1$). All the models show subdiffusive

dynamics at the intermediate time scale at low temperature, and this time regime becomes longer as temperature decreases. The rotational diffusion, however, is quite different from the translational one in that the subdiffusive regime is much shorter for the former at low temperature. The time scales represented by ISFs are comparable to those by MSDs (Figure 5.5), in that the process at the short time decay falls into the ballistic regime, the long relaxation time corresponds to the diffusive regime, and the plateau at the intermediate time scale is attributed to the subdiffusive motion.

This subdiffusive behavior is one of distinct properties of glass formers, and has been perceived as being ascribed to a multiple step process. When a particle is trapped in a cage by other particles, it takes time to escape, which causes the subdiffusive dynamics.[15,16,18,76] According to simulation studies on IL systems,[16,17] the dynamics becomes heterogeneous at the time scale a particle is about to escape the cage. From this context one may expect that the rotational motion shows less heterogeneous dynamics.

It is obvious that the Coulomb interaction makes the dynamics slower comparing the ISFs and the MSDs knowing from the temperature range of IL models and UCM. Comparing the translational motion of the two IL models, SCM is faster than that in ACM at the same temperatures. Since the masses and the molecular geometry of each species for both models are set to be the same, the difference of the translational motion is mainly due to the difference in the molecular charge distribution in a cation. It is notable that in the experiment study the relative diffusion constants of cations in systems having cations with charge delocalized,[69] such as 1-butyl-3-methylimidazolium and 1-butylpyridinium ions, are greater than those in systems with charge localized, such as *N*-butyl-*N*-methylpyrrolidinium and

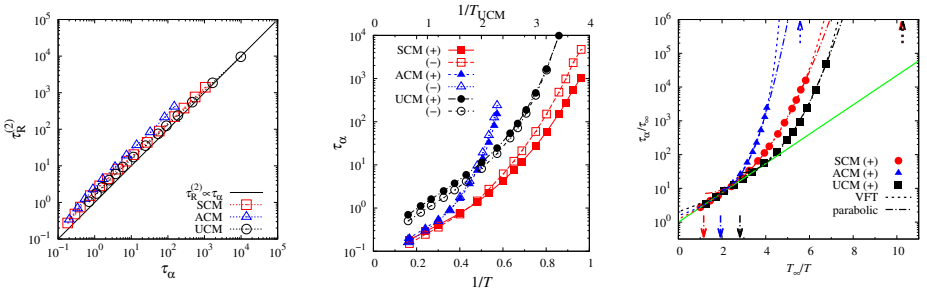

Figure 5.6: Left: $\tau_{\mathrm{R}}^{(2)}$ is scaled by $\tau_\alpha(q^*)$ very well: $\tau_{\mathrm{R}}^{(2)} \propto \tau_\alpha^1$. The reorientational and the structural relaxation is coupled very well. Center: $\tau_\alpha(q^*)$ is plotted versus $1/T$. (+) and (−) respectively indicate the cation and the anion. The temperatures for UCM is indicated at the top scale. Right: At high temperature $\tau_\alpha(q^*)$ and T are fitted by the Arrhenius law, $\tau_\alpha = \tau_\infty \exp[T_\infty/T]$. ACM looks the most fragile. The arrows at the bottom indicate the onset temperature for the parabola fitting, and the arrows at the top indicate the singular point from the VFT fitting.

N-butyl-N,N,N-trimethylammonium.

Comparing the structural relaxation time of each ion species, the anion, having the smaller size than the cation, relaxes faster than the latter at high temperature of all models (see Figure 5.4). With cooling down the anion relaxes more slowly than the cation for IL models, and the relaxation of both species for UCM collapses. The faster relaxation of the cation in ILs is consistent to previous studies.[8,12,74] Since the geometry and all the other parameters are the same for all the models, this discrepancy between the ion species of ILs is attributed to the charge distribution.

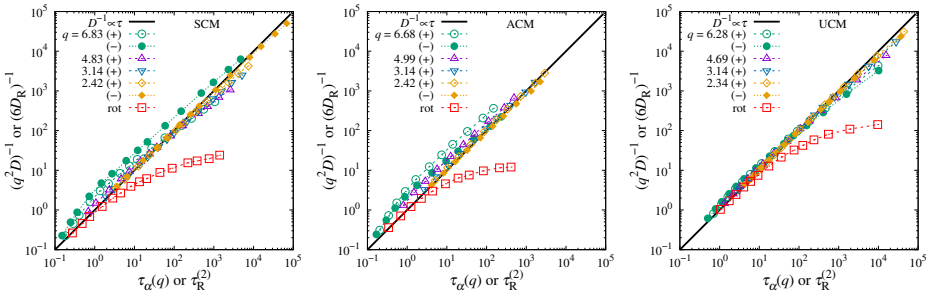

Figure 5.7: The scaling relation, $D \sim \tau_\alpha^{-\zeta_D}$, shows weak violation of the SE relation with the exponents, ζ_D between 0.75 and 0.9 at low temperature and at the short length scale, $q = q^*$. As the length scale becomes longer the SE relation recovers. D_R is much more decoupled from $\tau_R^{(2)}$ than the breakdown of the translational SE relation. q values are noted in the figure, and for brevity only the shortest and the longest length scales are indicated for the anion.

On the other hand, the MSD in ACM shows quite a different trend from the ISF. The diffusive motion of the anion is faster than the cation, and the reverted trend at the subdiffusive regime occurs only at low temperature. Since in typical ILs the cation has greater D than the anion,[8,69] the ACM is considered as an extreme case in charge distribution.

Figure 5.7 shows the breakdown of the SE relation at low temperature. Dynamic heterogeneity induced by the correlated motion of mobile particles, or hierarchical nature of dynamics can explain this breakdown.[42,47] At $T \approx 2$ for IL models and $T \approx 0.6$ for UCM, the diffusion constants, D and D_R, and the relaxation times, τ_α and $\tau_R^{(2)}$, start decoupling with temperature

decreasing. It is noticeable that the temperatures at which the diffusion constant and the relaxation time start to decouple fall into those where the subdiffusive regime starts to arise apparently.

This weak violation of the SE relation gives them the scaling exponent values between 0.75 and 0.9 at low temperature, via $D \sim \tau_\alpha^{-\zeta_D}$, and the values of ζ_D are shown in Figure 5.7. At long length scale translational motion converges to the Fickian diffusion, which has been considered as homogeneous dynamics. The rotational diffusion, however, show strong decoupling between D_R and $\tau_R^{(2)}$. While $\tau_R^{(2)}$ show similar trend with τ_α (Figures 5.4 and 5.6), the rotational diffusion at low temperature does not become as slow as the translational one (Figure 5.5). With this strong violation of the DSE relation one might interpret the rotation motion is more dynamically heterogeneous than translation motion. This is unveiled in the next section.

5.3 Dynamic heterogeneity

Previous studies have calculated for τ_{dh} from a differently defined correlation function, $\Delta(t_w)$, by integrating $F_4(\tau_1, t_w, \tau_2; q)$ over τ_2,[32,34]

$$\Delta(t_w; q, \tau_1) = \int_0^\infty d\tau_2 \left[\frac{F_4(\tau_1, t_w, \tau_2; q)}{F_s(q, \tau_1)} - F_s(q, \tau_2) \right], \tag{5.8}$$

which measures the difference between the filtered dynamics and the bulk dynamics. The time scale of dynamic heterogeneity, $\tau_{dh}^{(\Delta)}$, from Eq. (5.8) is defined as $\Delta(t_w = \tau_{dh}^{(\Delta)})/\Delta(0) = 1/e$. Otherwise defined time scale of dynamic heterogeneity has been employed in other studies.[24,28] One can replace $\Delta(\tau_{dh}^{(\Delta)})/\Delta(0)$ with the one obtained by integrating the 3TCF over both τ_1 and τ_2,[24,28]. We check in the insets of Figure 5.8 the consistency

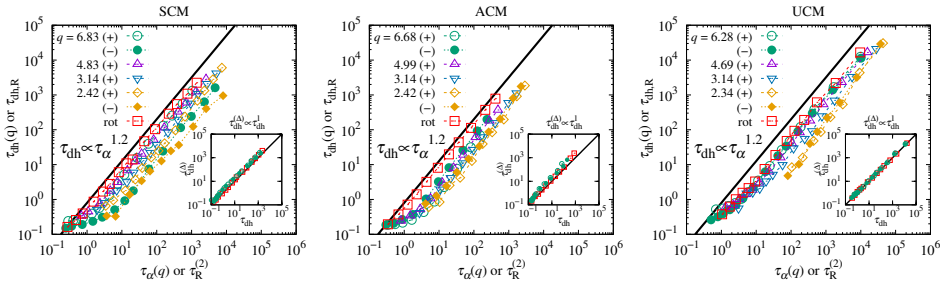

Figure 5.8: $\tau_{\rm dh}$ can be scaled by τ_α through the scaling relation $\tau_{\rm dh} \propto \tau_\alpha^{\zeta_{\rm dh}}$, where all the systems (left: SCM, center:ACM, right: UCM) have similar scaling exponent, $\zeta_{\rm dh} \approx 1.2$. The solid line is a guide. For the anions, only the longest and the shortest length scale are plotted for brevity, but the trend is the same as for the cations. (Insets) $\tau_{\rm dh}^{(\Delta)} \propto \tau_{\rm dh}$ at all systems with $q = q^*$ except at the lowest temperature of ACM showing a little discrepancy. It is ascribed to the statistical error of $\tau_{\rm dh}^{(\Delta)}$ since it needs longer trajectories to integrate (see Eq. (5.8)).

between the two time scales, $\tau_{\rm dh}^{(\Delta)} \propto \tau_{\rm dh}$, and we expect that the time scales in Refs. 24 and 28 will show the same relation. Rotational motion shows a little discrepancy at ACM, but it is ascribed to the statistical error of $\tau_{\rm dh}^{(\Delta)}$ since it needs longer trajectories to integrate. We, therefore, choose $\tau_{\rm dh}$ for the characteristic time scale of dynamic heterogeneity in further discussion.

Consequently, the relation between $\tau_{\rm dh}$ and τ_α, is obtained in Figure 5.8. From the results of D and the τ_α ACM shows slower dynamics, leading us to expect that $\tau_{\rm dh}$ of ACM will be greater than that of SCM and UCM, thus greater dynamic heterogeneity. When the models are compared at the same

temperatures, it seems as if charge induced the dynamic heterogeneity and as if asymmetry in charge distribution strengthened it.[13] τ_{dh}, however, can be scaled by τ_α through the scaling relation $\tau_{\mathrm{dh}} \propto \tau_\alpha^{\zeta_{\mathrm{dh}}}$, where $\zeta_{\mathrm{dh}} \approx 1.2$ in all the systems: ACM at the shortest length scale, $q = q^*$, may seem an exception with a bit greater value, but it converges to ≈ 1.2 at longer length scales.

It is noteworthy that UCM is another kind of 50/50 binary mixture glass-forming liquids, some of which have been widely used as model systems[24,25,33,47,86] to study glassy dynamics. The most distinctive feature of UCM from the others is that the cation is made up of two components. As other binary mixture models UCM shows heterogeneous dynamics, and its heterogeneity does not change by assigning charges into its component because the dynamics of both SCM and ACM are not much different from that of the uncharged counterpart, UCM, if the temperatures are rescaled (see Figure 5.6), and all the models have the same exponent, ζ_{dh}. It was reported the time scales of dynamic heterogeneity have different scaling behavior with respect to τ_α when the types of short-range interaction differ.[24] Since the short-range interaction and the structure of the models in this study are the same, we believe that dynamic properties are not affected by long range interaction, but rather by the molecular structure, which are determined by short range interaction.[8]

As atomistic models, the results of binary mixture glass systems are worth while to be compared although the definitions of τ_{dh} were a little different. Ref. 33 found the exponent ≈ 1.08 for the soft sphere model using a 3TCF with a correlator different from the one used in this study. Ref. 24, where the 3TCF similar to that in this study was employed, manifested

that the fragile liquids have greater values of $\zeta_{\rm dh}$ than the strong liquid, *e.g.*, $\zeta_{\rm dh} \approx 1.25$, 1.9, and 1.5 for the fragile liquids: Kob-Andersen, Wahnström model, and the soft sphere models, respectively, while a strong liquid model mimicking SiO_2 shows $\zeta_{\rm dh} \approx 0.9$. This power-law relation is a general phenomenon in all the above models including the three models studied in this dissertation. The scaling relation is also comparable to that of KCMs, which are spin models for supercooled liquids. According to the study in Ref. 32, for both strong and fragile models $\zeta_{\rm dh} \approx 1$, where they showed that a fragile system displays slightly more heterogeneous dynamics: 1.06

Table 5.1: Comparison of the exponent, $\zeta_{\rm dh}$, values with other models

$$\tau_{\rm dh} \propto \tau_{\alpha}^{\zeta_{\rm dh}}$$

Models	IL/UCM[a]	Wahn[b]	WCA[c]	KA[b]	SS[b]	SS[d]	NTW[b]	KCM[e]
$\zeta_{\rm dh}$	1.2	1.9	1.4	1.25	1.5	1.1	0.9	1[d]

[a] IL models include SCM and ACM. All the models studied in this study have the same exponent.

[b] Ref. 24. KA: Kob-Andersen 80/20 LJ binary mixture, Wahn: Wahnström 50/50 LJ binary mixture, SS: Soft sphere 50/50 soft core binary mixture, NTW: tetrahedral network-forming 1:2 mixture

[c] Wahnström model modified with the WCA potential, obtained from Section 4.2.3.

[d] Ref. 33. SS: the same model as SS in Ref. 24 with $\tau_{\rm dh}$ calculated from a different correlator

[e] Ref. 32. $\zeta_{\rm dh} = 1.06$ for the East model, a KCM for a fragile liquid, and 0.98 for the FA model for a strong liquid.

for the fragile liquid and 0.98 for the strong liquid. The models studied in this dissertation are all fragile and have the value of $\zeta_{\rm dh} > 1$ that they do not show inconsistent results to the trend between the fragility and $\zeta_{\rm dh}$. The exponent values are summarized in Table 5.1.

The length scale dependence on the SE relation and $\zeta_{\rm dh}$ is investigated in the binary glass-forming liquids from Section 4.2. In Figure 5.9 all the models show weak violation of the SE relation at a short length scale, $q \sim q_0$, and the Fickian diffusion recovers at longer length scale. We again found the universal power-law behavior: $\tau_{\rm dh} \propto \tau_\alpha^{\zeta_{\rm dh}}$, and $\zeta_{\rm dh}$ does not change with the length scales. The results are consistent to the IL models and UCM.

Moreover, in the perspective of dynamic heterogeneity time scale, it is also notable that translational and rotational motions are strongly coupled, both having the same exponent, $\zeta_{\rm dh}$, despite the strong decoupling in diffusion between the two motions (see Figures 5.7 and 5.8). For the discussion on this we employ a previous study on supercooled model system with dumbbell molecules,[44] where the authors ascribed this inconsistency to the inadequacy of the definition, Eq. (A.1). They found that $\left\langle \Delta\phi^2(t) \right\rangle$ increases diffusively even when the orientation of the molecule is actually trapped and doing librational motion. This leads decoupling between $D_{\rm R}$ and D with the former increasing further. It needs in-depth investigation to tell if this interesting discrepancy comes from real physics or contribution from the librational motion in rotational dynamics. Nevertheless, we used this definition because there is no other way, at the present, of calculating angular displacement unboundedly. If the librational motion were possible to be expressed in a proper way, excluding the librational motion from stacking fallaciously to increase MSAD continuously, the breakdown

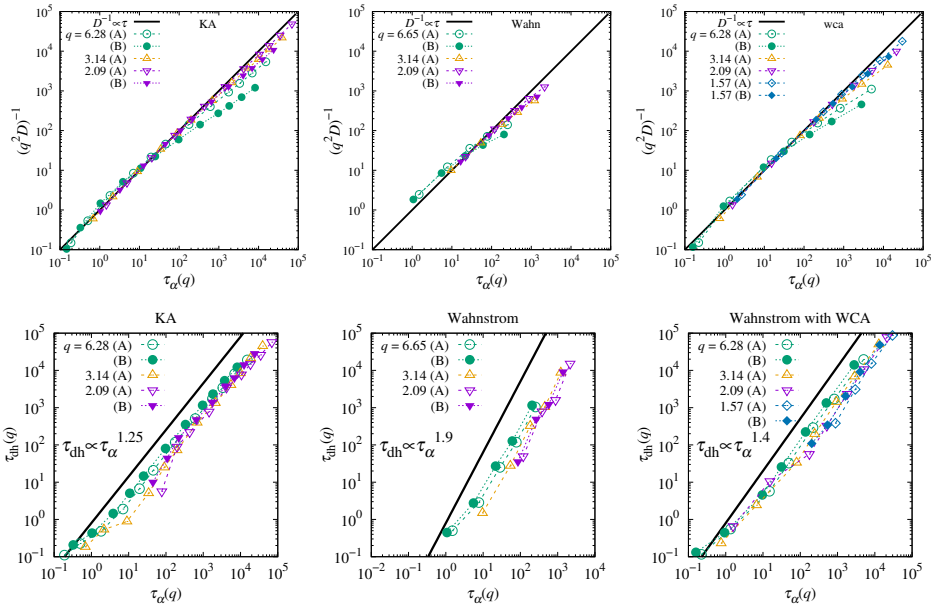

Figure 5.9: Comparison to the glass-forming binary mixture models introduced in Section 4.2. The scaling relation, $D \sim \tau_\alpha^{-\zeta_D}$, shows weak violation of the SE relation. As the length scale becomes longer the SE relation recovers. q values are noted in the figure, and for brevity only the shortest and the longest length scales are indicated for the anion. τ_{dh} can be scaled by τ_α through the scaling relation $\tau_{dh} \propto \tau_\alpha^{\zeta_{dh}}$, where all the systems (left: KA, center:Wahnström, right: Wahnström with WCA) do not change their exponent, ζ_{dh} with different length scales, q. The solid line is a guide. For the small particles, denoted by (B), only the longest and the shortest length scale are plotted for brevity, but the trend is the same as for the cations.

of the DSE relation would not be that severe.

Now, it seems appropriate to note an interesting finding that the length scale of structural relaxation reflects very little the dynamic heterogeneity, in contrast to the breakdown of the SE relation (see Figures 5.7 and 5.9). As the length scale increases, the ISFs become exponential and the diffusion and the structural relaxation are coupled. From this perspective it should follow the dynamics of Brownian motion at a long length scale. Time scale of dynamic heterogeneity studied in this dissertation, however, maintains the same exponent regardless of the length scale. It persuades us to believe that the dynamics is Fickian at the long length scale but still heterogeneous although we did not capture a tangible evidence as in Ref. 55. It is obvious that τ_{dh} is a characteristic time scale of dynamic heterogeneity that is distinguished from the two-point time scales, τ_α and $\tau_{\mathrm{R}}^{(2)}$.

Chapter 6

Conclusions

We investigated how the charge distribution on ions and the length scale of the structural relaxation effects the dynamic properties and the dynamic heterogeneity of IL systems by performing the molecular dynamics simulations on two simple models of ILs and their neutral counterpart: symmetric-charge model (SCM), asymmetric-charge model (ACM), and uncharged model (UCM). We found that all the models maintain amorphous liquid structures, and they show nonexponential relaxation and subdiffusive behavior at low temperatures.

Coulomb interaction lowers the temperature at which glassy dynamics appears, and the asymmetry in charge distribution provokes the time scale of dynamics longer. SCM shows similar dynamic properties of typical ILs in that the cation shows faster process than the anion in both structural relaxation and diffusion. Relations between τ_α and temperature show that all models behaves like fragile liquids. The SE relation breaks down at short length scales, and it recovers as the length scale increases. The rotational motion, however, shows strong decoupling between the diffusion and the

relaxation time: strong breakdown of the DSE relation.

We correlated a four-point correlation function to its two-point correlation function by adopting the 3TCF, analogously to the conventional four-point correlation function. The lifetime, τ_{dh}, of dynamic heterogeneity defined from the 3TCF, scales very well with the time scale, τ_α, of the two-point correlation function: $\tau_{\mathrm{dh}} \propto \tau_\alpha^{\zeta_{\mathrm{dh}}}$ with $\zeta_{\mathrm{dh}} \approx 1.2$, which holds for both the translational and the rotational correlation functions with the same exponent. This power-law relation is a general phenomenon in glass-forming liquids, similar to the relation between ξ_{dh} and τ_α, although the exponent is dependent on the models from other studies: fragile liquids have greater values than strong liquids. The rotational dynamics also shows the same dynamic heterogeneity giving the same ζ_{dh} value despite the strong breakdown of DSE relation. It is apparent that the time scale of dynamic heterogeneity is a distinctive time scale from the two-point correlation functions, such as the structural relaxation and the rotational relaxation.

The exponent, ζ_{dh}, is irrelevant to the charge distribution on the molecule, type of interactions, and even the length scales of the two-point correlation function. With the longer length scale the structural relaxation is detected, the more it becomes Fickian while the dynamics is seemingly maintaining its heterogeneity. We expect that our results provide useful insight on the relation between the dynamic heterogeneity and the types of molecular interaction although the 3TCFs need more theoretical supports compared to the conventional four-point correlation function. The length scale and other properties of dynamic heterogeneity of these models are to be obtained in our further study.

Part II

Electric Double Layer Capacitors with Ionic Liquids and Graphene Oxide

Chapter 7

Introduction

Electric double layer capacitors (EDLCs), or supercapacitors, are promising devices having high power density and energy density.[90] What provides them with high capacitance is electric double layer formed at electrode surface, and it completely screens at sub-nanometer length scale the electric potential applied by the electrodes.[90–94] The electric double layer being crucial for an EDLC's high capacitance, it has ionic species either in aqueous or organic electrolyte. Another class of electrolytes used in EDLCs is ionic liquids (ILs), which are mostly made up of bulky cations and small symmetric anions, *e.g.*, 1-ethyl-3-methylimidazolium tetrafluoroborate ($EMI^+BF_4^-$). Although ILs are considered as green alternative to toxic, volatile conventional organic solvents, their high viscosity makes them electrically less conductive. ILs mixed with acetonitrile, a conventional organic electrolyte, have been used in order to improve the electric conductivity.[90,94–100]

Another important component of supercapacitors, critical for EDLC performance, is electrodes. Graphene-based materials have received extensive scrutiny due to their excellent properties, including high stability, electri-

cal conductivity, surface area, and electrolyte wettability.[94,101,102] Many simulation studies have been performed by modeling pristine graphenes with IL electrolyte,[93,98–100,103–106] as well as experimental studies.[107–111] Graphene oxide (GO), however, has not been investigated thoroughly in simulation studies of EDLCs while it has become an experimentally "hot" materials in recent studies[57,59–67,112–117] due to the fact that oxygen impurity is likely introduced in the process of reducing graphene oxide to make pristine graphene.[118,119]. It turned out that hydrogen bonding between the oxygen impurity in GO electrodes and the electrolyte molecules is one of the main factors that affects the capacitance.[57,116,117]. The results on capacitance are, however, controversial; while some measurements suggest that oxidation enhances capacitance,[59,60] others indicate that GO has lower capacitance than pure graphene.[61–67] Computer simulations have mainly focused on pure graphene systems.[93,98–100,103–106]

We firstly reported the computational study on the interfaces between GO and liquid by varying the configuration on the GO electrodes,[57] where the electrode oxidation was controlled by the concentration of hydroxyl groups (-OH) on the GO surface, whereas many other computational studies[120–126] which have investigated the properties of GO itself. Very recent MD studies with GO electrodes[57,116,117] show that capacitance decreases with increasing electrode oxidation. In this study, we compare IL-based GO supercapacitors[57] to OE-based systems. Screening mechanisms of electrode charges, their variations with electrode oxidation and influence on capacitance are analyzed. Comparison of IL and OE systems is made.

The remainder of Part II is outlined as follows. Chapter 8 is devoted to model descriptions and simulation methods. In Chapter 9, we present our

main results on structural properties in the model systems, and discuss our finding. Finally, we summarize the results and conclude in Chapter 10.

Chapter 8

Models and simulation methods

The simulation system, consisting of an electrolyte confined between two GO electrodes in the parallel-plate configuration (Figure 8.2), is the same as in our previous work.[57] Two different types of electrolytes, a pure ionic liquid (IL) and an organic electrolyte (OE), were considered.[57,98–100] The IL system comprises 256 pairs of $EMI^+$and BF_4^- ions, while the OE system is composed of 62 $EMI^+BF_4^-$ pairs and 634 acetonitrile molecules, corresponding to a $\sim 1.3\,\mathrm{M}$ solution of $EMI^+BF_4^-$. The supercapacitor system with IL ("IL supercapacitor") was studied in detail in our previous work.[57] Therefore, in the present paper, we will focus mainly on the supercapcitor with OE ("OE supercapcitor") and give only the highlights of the IL supercapacitor results to show the aspects shared by and the contrasts with the OE supercapacitor.

The model descriptions employed here are identical to those of Ref. 57. Specifically, two GO electrodes, each modeled as a flat, rigid graphene sheet with area $3.396 \times 3.431\,\mathrm{nm}^2$, are separated by $d(= 6.6\,\mathrm{nm})$ and situated at $z = \pm z_0$ ($z_0 = 3.3\,\mathrm{nm}$) parallel to the xy-plane. Each electrode consists

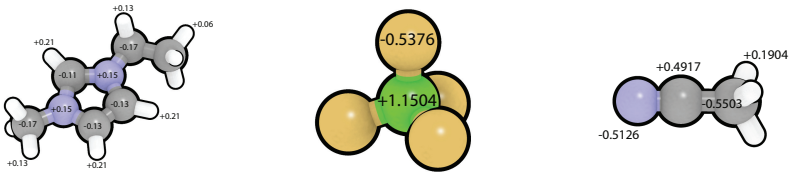

(a) EMI^+ (b) BF_4^- (c) CH_3CN

Figure 8.1: Structure and partial charges of each species of the electrolyte. All equivalent H or F atoms have the same partial charges.

of 448 carbon atoms and is decorated by hydroxyl (–OH) moieties, which are the sole oxidative groups in our model. We use C_{ox} and C_{un} to denote oxidized carbon atoms (that are directly bonded to hydroxyl oxygen atoms) and unoxidized carbon atoms of GO, respectively. The OH groups are placed in adjacent pairs with the O-C_{ox}-C_{ox}-O dihedral in a *trans* conformation. Two C_{ox} atoms of each oxidized pair are shifted by 0.1 Å toward each other and positioned off the graphene plane by 0.4 Å in the direction of their respective OH groups. The OPLS–AA force field[127] was used to describe the hydroxyl groups and C_{ox} atoms, while the Lennard-Jones (LJ) parameters of Ref. 128 were employed for C_{un}. For IL, the parameters for EMI^+ were taken from Refs. 83 and129, while those for BF_4^- were from Refs. 130 and131. For CH_3CN, the fully flexible six-site description of Ref. 132 was employed.

Molecular dynamics simulation protocols employed here are detailed in Ref. 57. Briefly, system nuclear dynamics were simulated in an orthorhom-

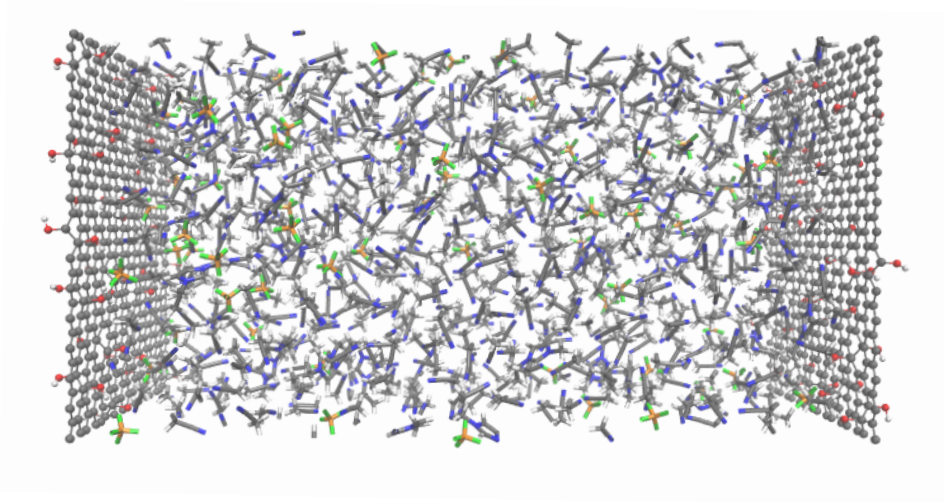

Figure 8.2: Model EDLC with an organic electrolyte composed of EMI^+, BF_4^-, and CH_3CN. GO electrodes on the left (anode) and right (cathode) are charged with $+5e$ and $-5e$, respectively. Both electrodes are 10% oxidized.

bic box with dimensions $3.396 \times 3.431 \times 30.0\,\mathrm{nm}^3$ in the canonical ensemble at 350 K using the GROMACS program.[133] Long-range electrostatic interactions were computed using the particle-mesh-Ewald method with a 2D correction factor.[134] The GO electrodes were uniformly charged by assigning partial charges to the carbon atoms, so that surface charge densities of $\sigma_S = 0, \pm 0.215$, and $\pm 0.43\,e/\mathrm{nm}^2$—corresponding to total electrode charges of 0, ± 2.5 , and $\pm 5\,e$—were achieved (e = elementary charge). The electrode located at $z = -z_0$ (electrode 1) was charged positive while the electrode at z_0 (electrode 2) was charged negative. At least ten different trajectories were simulated for each charged supercapacitor. In the discharged case,

five trajectories were simulated. For each trajectory, simulation was carried out with 6 ns of annealing from 700 K to 350 K and 4 ns of equilibration at 350 K, followed by a 10 ns production run. Ensemble averages were computed using ten independent 10 ns production trajectories thus generated for the charged case and five trajectories for the discharged case.

Chapter 9

Results and discussion

9.1 Overall properties of the GO supercapacitors with oxidation

We begin our analysis by considering the electric potential and specific capacitance of the GO supercapacitors. The half-cell potential $\Delta\Phi_i$ (i = anode, cathode) and cell voltage $\Delta\Phi^{\text{cell}}$ are defined as

$$\begin{aligned}
\Delta\Phi^{\text{anode}} &= \Phi(z=-z_0) - \Phi(z=0); \\
\Delta\Phi^{\text{cathode}} &= \Phi(z=0) - \Phi(z=z_0)\ ; \\
\Delta\Phi^{\text{cell}} &= \Phi(z=-z_0) - \Phi(z=z_0) = \Delta\Phi^{\text{anode}} + \Delta\Phi^{\text{cathode}}\ . \qquad (9.1)
\end{aligned}$$

Here $\Phi(z)$ is the electric potential at z calculated by integrating the Possion equation [91,93]

$$\begin{aligned}
\Phi(z) &= -4\pi \int_{-\infty}^{z} dz'\,(z-z') \sum_{\alpha}^{\text{all}} \bar{\rho}_\alpha(z')\ ; \qquad (9.2) \\
\bar{\rho}_\alpha(z) &= A_0^{-1} \int_{-x_0}^{x_0}\int_{-y_0}^{y_0} dx'dy'\,\rho_\alpha(x',y',z)\ ,
\end{aligned}$$

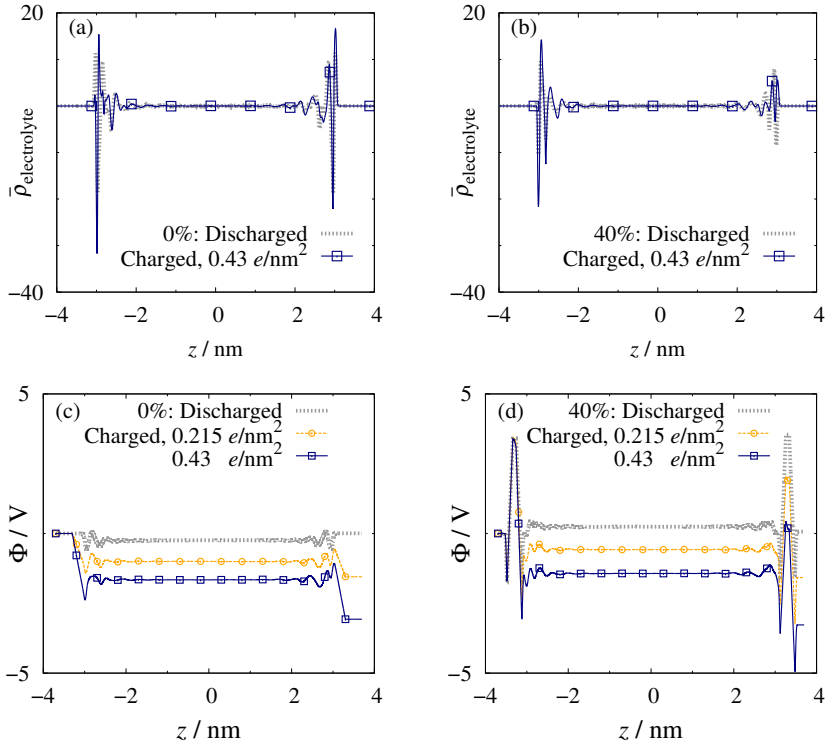

Figure 9.1: Charge density profiles with neat graphene electrodes (a) and 40%-oxidized GO (b), where $\sigma_{\mathrm{S}} = \pm 0.43\, e/\mathrm{nm}^2$. Electric potential profiles with neat graphene electrodes (c) and 40%-oxidized GO (d). Discharged data are plotted in thick gray dotted lines, $0.215\, e/\mathrm{nm}^2$ in with dashed lines with open circles, and $0.43\, e/\mathrm{nm}^2$ in solid lines with open squares.

where $\rho_\alpha(x', y', z)$ is the local charge density of species α ($\alpha = \mathrm{EMI}^+$, $\mathrm{BF_4}^-$, $\mathrm{CH_3CN}$, or electrode) at position (x', y', z), $\bar{\rho}_\alpha(z)$ is its average over x and y, $\sum_\alpha^{\mathrm{all}}$ is the sum over all species, and $A_0 = 4x_0y_0$ is the electrode surface

area.

The profiles of $\bar{\rho}_{\text{electrolyte}}(z)$ and $\Phi(z)$ for the charged and discharged supercapacitors at selected oxidations are illustrated in Figure 9.1, where the former is the sum of $\bar{\rho}_\alpha(z)$ (α = EMI^+, $BF_4{}^-$, and CH_3CN). When the capacitor with neat graphene is discharged, the Φ near both electrodes is symmetrical while with 40%-oxidized GO discharged Φ is biased to one side due to its random configuration of hydroxide groups on GO. When the electrodes are charged, the charge density of electrolyte with both neat and GO have plateau regime, *i.e.*, potential of zero charge (PZC), far from the electrodes. We found that all the capacitor systems in this study show this plateau. The symmetric charge density with discharged neat graphene electrodes changes along with charging. $\bar{\rho}$ of all cases show layered structure near electrodes. The charges of electrolyte shield the electric potential exerted by the electrodes in a very short range of distance, $\approx$ 1 nm from the electrodes.

The area-specific capacitance, $c_{\text{S}}^{\text{tot}}$, defined as the capacitance of the cell, normalized to the electrode surface area A_0, is given by

$$c_{\text{S}}^{\text{tot}} = \frac{|\sigma_{\text{S}}|}{\delta\Delta\Phi^{\text{cell}}} \; ; \qquad c_{\text{S}}^{i} = \frac{|\sigma_{\text{S}}|}{\delta\Delta\Phi^{i}} \; ; \qquad \frac{1}{c_{\text{S}}^{\text{tot}}} = \frac{1}{c_{\text{S}}^{\text{anode}}} + \frac{1}{c_{\text{S}}^{\text{cathode}}} \; , \tag{9.3}$$

where c_{S}^{i} (i = anode, cathode) is the area-specific electrode capacitance. The capacitance of the total cell of both capacitors with $\sigma_{\text{S}} = 0.43$ and $0.215\, e\,\text{nm}^{-2}$ are plotted in Figure 9.2, and the values of total and half cells' capacitance with $\sigma_{\text{S}} = 0.43\, e\,\text{nm}^{-2}$ are listed in Table 9.1.

Figure 9.2 presents the simulation results of the electric potential drops, $\delta\Delta\Phi^{\text{cell}}$ of each half cell, where δ denotes the difference of the charged and discharged cases, for example, $\delta\Delta\Phi^{\text{cell}} = \Delta\Phi^{\text{cell}}$ (charged)$-\Delta\Phi^{\text{cell}}$ (discharged).

Table 9.1: MD results for specific capacitance of graphene oxide supercapacitors†

	IL			OE		
Oxidation	$c_{\mathrm{S}}^{\mathrm{tot}}$	$c^{(+)}$	$c^{(-)}$	$c_{\mathrm{S}}^{\mathrm{tot}}$	$c^{(+)}$	$c^{(-)}$
0%	2.60	4.88	5.56	2.24	4.87	4.14
5%	2.35	4.85	4.57	2.26	4.86	4.25
10%	2.30	4.73	4.49	2.22	4.66	4.17
20%	2.31	4.96	4.33	2.22	4.62	4.28
25%	2.26	4.83	4.24	2.23	4.55	4.36
30%	2.25	4.49	4.53	2.23	4.33	4.58
40%	2.18	4.31	4.43	2.10	4.29	4.12
60%	2.04	4.06	4.12	1.98	4.04	3.91
70%	1.94	3.75	4.02	1.84	3.90	3.49
80%	1.94	3.83	3.94	1.81	3.85	3.41
100%	1.86	3.63	3.86	1.72	3.72	3.20

† Units: $\mu\mathrm{F\,cm^{-2}}$. $c_{\mathrm{S}}^{\mathrm{tot}}$, $c_{\mathrm{S}}^{(+)}$, and $c_{\mathrm{S}}^{(-)}$ are the surface area-normalized capacitance for the whole capacitor, the anode, and the cathode, respectively.

For both IL and OE supercapacitors, $\delta\Delta\Phi^{\text{cell}}$ generally increases with the increasing oxidation of the GO electrodes. In our previous work, this trend for the IL supercapacitors was attributed to two factors, *i.e.*, decreasing reorganization ability of IL ions and widening gap of double layers as the electrode oxidation increases.[57] One of the most salient features of Figure 9.2a is the large difference in $\delta\Delta\Phi^{\text{cell}}$ at 0 and $\sim$ 100 % electrode oxidation between the two electrolytes we considered. As a consequence, $\delta\Delta\Phi^{\text{cell}}$ and $c_{\text{S}}^{\text{tot}}$ for the IL supercapacitor show, respectively, a rapid increase and decrease from 0 to $\sim$ 10% oxidation, while those for the OE supercapacitor remain nearly constant at low electrode oxidation.

The analysis of the half-cell potentials in Figure 9.2c and d reveals that the origin of the pronounced difference in $\delta\Delta\Phi^{\text{cell}}$ between the two electrolytes at low and high electrode oxidation is the positively-charged cathode. The anode potential with respect to the potential of zero charge (PZC), viz., discharged electrode, for the OE and IL supercapacitors shows nearly an identical behavior; it increases almost linearly with the % oxidation of the GO electrodes. By contrast, $\delta\Delta\Phi^{\text{cathode}}$—the magnitude of the cathode potential with respect to PZC—shows a markedly different behavior between the IL and OE. Specifically, $\delta\Delta\Phi^{\text{cathode}}$ for the IL supercapacitor increases rapidly from 0 to 25 % oxidation, whereas it decreases slightly for the OE supercapacitor. Above 30 %, OE exhibits more rapid increase in $\delta\Delta\Phi^{\text{cathode}}$ than IL.

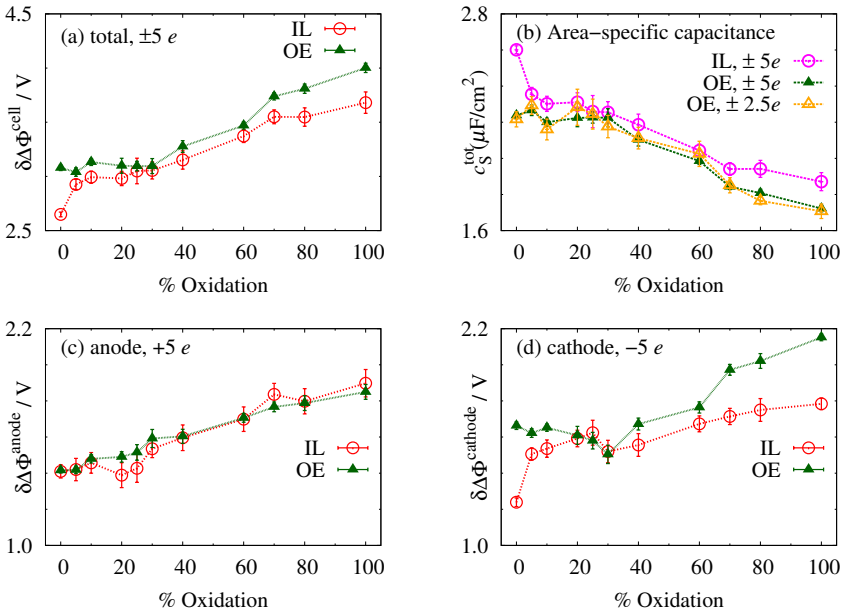

Figure 9.2: The total electric potential drop (a), $\delta\Delta\Phi^{\text{cell}}$, of IL supercapacitor (open circle) and OE supercapacitor (filled triangle) vs. % oxidation and the total capacitance (b), $c_{\text{S}}^{\text{tot}}$, converted from $\delta\Delta\Phi^{\text{cell}}$. The open triangle is plotted for $\sigma_{\text{S}} = \pm 0.215\, e\,\text{nm}^{-2}$ case. The potential drop of the half cell, the anode (c) and the cathode (d), $\delta\Delta\Phi_{\text{half}}$ vs % oxidation. Error bars mark $\pm\sigma$, where σ is one standard deviation.

9.2 Hydrogen bonding at the screening zone

The cathode-anode asymmetry in the half cell potential is usually ascribed to differing screening ability of ions, which depends on factors, such as ion size, shape and charge distribution.[91,98–100,135] While previous computational works focused mostly on counter-ions and their influence on the

cathode-anode asymmetry, our prior analysis has suggested the importance of co-ions for IL.[57] A recent NMR study of microporous carbon supercapacitors also indicates that co-ions can contribute to electrode screening by "desorbing" from the electrode.[136] Here we examine respective roles played by counter-ions and co-ions in electrode charge screening. In order to do so, we analyze numbers of cations and anions (and also CH_3CN molecules in the case of OE) in the screening zone (SZ), defined as the interfacial electrolyte region in which the ion number difference between the counter-ions and co-ions is the same as the magnitude of the electrode charge in units of e.[98]

The MD results for the ion population in SZ in the IL and OE supercapacitors are displayed in Figures 9.3 and 9.4, respectively. We first consider the IL case. For the discharged IL supercapacitor (Figure 9.3a), the numbers of the cations and anions in SZ do not vary with the degree of electrode oxidation. Because of local electroneutrality, the cation and anion populations in SZ are nearly the same. When the electrodes become charged, the populations of the counter-ions and co-ions in SZ increase and decrease, respectively, as expected. However, there is a notable disparity between the cathode and anode. Reorganization of ion populations in SZ in response to electrode charging occurs mainly via increase in counter-ions (BF_4^-) near the anode (Figure 9.3c), whereas both the counter-ions, EMI^+, and co-ions, BF_4^-, make important contributions at the cathode (Figure 9.3d). The important role played by BF_4^- in screening the cathode charge as co-ions in IL was also noted in our prior study.[57]

The situation is quite different for OE and several features are notewor-

[§]Adapted from Figure 4 of Ref. 57 with permission.

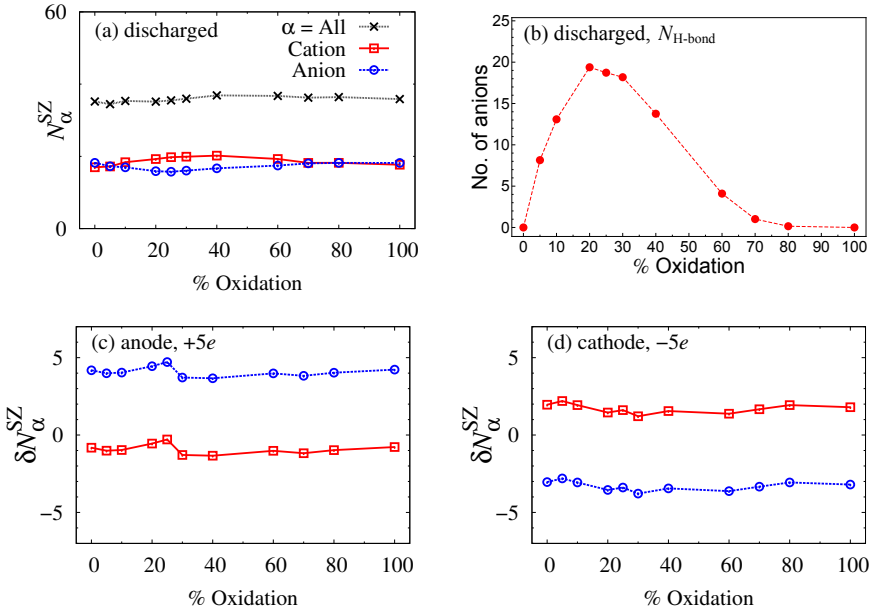

Figure 9.3: IL supercapacitor: (a) Number of molecules in the screening zone of the discharged cell. (b) Number of anions hydrogen bonded, $N_{\text{H-bond}}$, to OH groups of the electrodes.[§] (c-d) The change over charging in the number of molecules in the screening zone is defined as $\delta N_\alpha^{\text{SZ}} = N_{\alpha,\text{charged}}^{\text{SZ}} - N_{\alpha,\text{discharged}}^{\text{SZ}}$. The screening zone is defined to make difference in $\delta N_\alpha^{\text{SZ}}$ between the cation and the anion is 5, which ranges from $\Delta z \leq 2.7\,\text{nm}$ (0%) to $\leq 2.5\,\text{nm}$ (100%). See details in Table B.1.

thy. First, there is no appreciable ion population in the SZ of the discharged OE capacitor at 0 % oxidation because the ion concentration of OE is very low, compared to IL; thus the SZ is populated almost exclusively by acetonitrile (Figure 9.4a). Second, as the electrode becomes more oxidized by

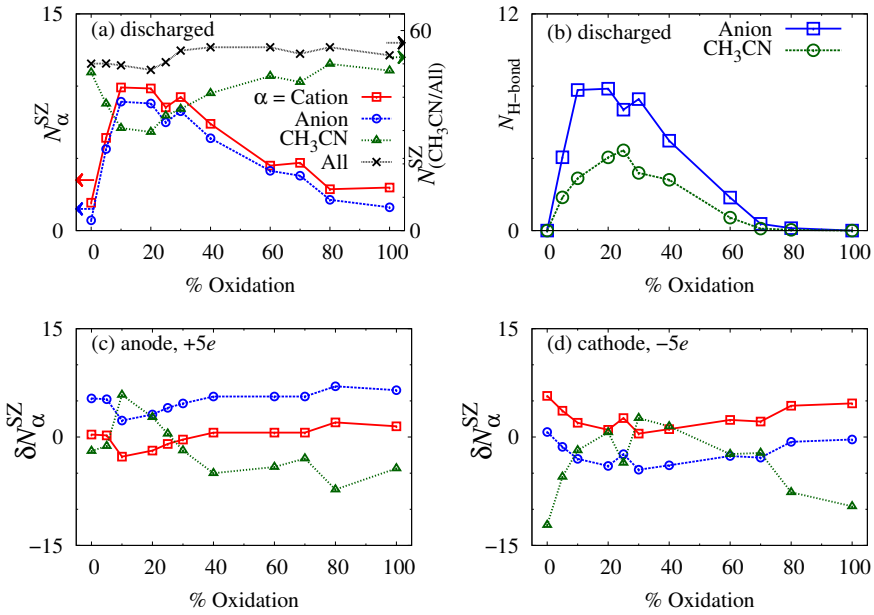

Figure 9.4: OE supercapacitor: (a) Number of molecules in the screening zone of the discharged cell. (b) Number of electrolyte species hydrogen bonded, $N_{\text{H-bond}}$, to OH groups of the electrodes. (c-d) The change over charging in the number of molecules in the screening zone is defined as $\delta N_\alpha^{\text{SZ}} = N_{\alpha,\text{charged}}^{\text{SZ}} - N_{\alpha,\text{discharged}}^{\text{SZ}}$. The screening zone is defined the same as in the IL case, Figure 9.3. See details in Table B.1.

adding OH groups to the graphene surface, the ion densities in the SZ initially grow, while acetonitrile shows the opposite trend. The formation of hydrogen bonds between the anions and the electrode OH groups is mainly responsible for the anion density increase (Figure 9.4b). This in turn increases the cation population in SZ to meet the local electroneutrality con-

dition. Beyond ~ 20 % oxidation, however, the number of anion-OH hydrogen bonds decreases analogous the IL case (Figure 9.3b). This is attributed to increasing steric hindrance between the anions and OH groups.[57] This results in the reduction of the anion and thus cation populations in the SZ. Our results indicate that the specific interactions between the GO surface and ions play a central role in determining the ion populations in SZ for the discharged OE supercapacitor.

Response of OE to electrode charging shows an interesting cathode-anode asymmetry, which is different from IL. At the anode, the ion density reorganization in SZ is effected primarily via the increase of counter-ions BF_4^- (Figure 9.4c). The exception is $\sim$ 10–30 % oxidation, where EMI^+ as co-ions also make a significant contribution presumably because the reorganization ability of BF_4^- is restricted due to the formation of a maximum number of hydrogen bonds with electrode OH groups. Nevertheless, the anion dominance in the ion density reorganization near the anode of the OE supercapacitor is similar to the IL case in Figure 9.3c.

By contrast, the reorganization mechanism of ion populations near the cathode of the OE supercapacitor varies with the electrode oxidation. Near the 0 % oxidation, the counter-ions, EMI^+, are mainly responsible for ion density change in SZ, *i.e.*, reorganization occurs via the influx of EMI^+ into SZ, induced by Coulomb attraction. Since co-ions BF_4^- are nearly absent in the SZ in the discharged case, they cannot contribute to screening of the negatively-charged cathode. As the electrode oxidation level increases, the co-ions play a progressively more important role because the BF_4^- population in SZ grows due to hydrogen-bonding interactions with OH groups of the cathode. As a result, between $\sim$ 20 and $\sim$ 80 % oxidation, both

cations and anions make a significant contribution to charge reorganization by moving into and moving out of the SZ region, respectively. As the cathode becomes further oxidized, the counter-ions become dominant again because of the significant lowering of the co-ion population. The GO oxidation-dependent co-ion contribution to the cathode screening of the OE supercapacitor is the major difference from the IL supercapacitor.

The analysis above sheds illuminating light on the disparity between the cathode and anode and the similarities and differences of the IL and OE. As noted above, the screening at the anode is mainly governed by BF_4^- through their population enhancement in SZ for both the IL and OE supercapacitors. This probably explains the similarity of $\delta\Delta\Phi^{\text{anode}}$ between the IL and OE supercapacitors ($\delta\Delta\Phi^{\text{cathode}}$). Furthermore, one can easily imagine that the anion density enhancement in response to the anode charging will become more difficult as more OH groups are added to the electrode surface. The presence of hydrogen-bonded anions and steric hindrance of OH groups provide a more rigid environment for new incoming anions to enter the SZ region as well as for existing anions to approach the electrode closely than the pure graphene electrode with no OH groups. As such, the screening efficiency of anions decreases with the increasing electrode oxidation.[57] This explains near linear increase of $\delta\Delta\Phi^{\text{anode}}$ in Figure 9.2c.

At the cathode, both cations and anions contribute to ion density reorganization in SZ for the IL supercapacitor as explained above. Therefore, upon charging, many anions (which are co-ions in this case) will move away from the cathode and out of the SZ. In the case of the oxidized cathode, this will involve breaking of several anion-OH hydrogen bonds. For pure graphene, on the other hand, the reorganization of anions would be much

easier because of the absence of hydrogen bonds. This difference in ease of ion reorganization is the likely reason for the abrupt increase in $\delta\Delta\Phi^{\mathrm{cathode}}$ and thus a large drop in screening efficiency from 0 to 5 % oxidation for the IL supercapacitor. Since the degree of anion hydrogen-bonding increases with the electrode oxidation up to $\sim$ 20 %, so does $\delta\Delta\Phi^{\mathrm{cathode}}$. At high electrode oxidation, a widening gap of double layers caused by steric hindrance arising from OH groups is believed to be mainly responsible for the $\delta\Delta\Phi^{\mathrm{cathode}}$ trend.[57]

In the case of the OE supercapacitor, the BF_4^- population near the electrode increases with the electrode oxidation in the low oxidation region (Figure 9.4a) thanks to the hydrogen-bond formation (Figure 9.4b) as noted above. Thus while the individual ions' reorganization ability may decrease, the number of anions that can contribute to the anode screening as co-ions increases with electrode oxidation. The initially decreasing trend of $\delta\Delta\Phi^{\mathrm{cathode}}$ in OE in Figure 9.2d indicates that the latter aspect, not shared by IL, is more dominant than the former. The large gap in $\delta\Delta\Phi^{\mathrm{cathode}}$ between the IL and OE supercapacitors at 0 % oxidation is attributed to the lack of the BF_4^- contribution due to its vanishing population in SZ of the OE supercapacitor. For $\gtrsim$ 60 % oxidation, $\delta\Delta\Phi^{\mathrm{cathode}}$ in OE increases more rapidly than that in IL because the BF_4^- population in SZ of OE decreases with increasing electrode oxidation (Figure 9.4a), another feature absent in IL (Figure 9.3a).

9.3 Screening by cations and anions at the screening zone

Our analysis thus far is based on the anion and cation numbers in SZ and their changes in response to electrode charging. For additional insight, we investigate how individual ionic species influence the system electric potential and screen the electrode charges. To do so, we consider the electric potential change due to the reorganization of species α

$$\begin{aligned} \delta\Phi_\alpha(z) &= -4\pi \int_{-\infty}^{z} dz'(z-z')\,\delta\bar{\rho}_\alpha(z') \ ; \\ \delta\bar{\rho}_\alpha(z) &\equiv \bar{\rho}_{\alpha,\text{charged}}(z) - \bar{\rho}_{\alpha,\text{discharged}}(z) \ . \end{aligned} \tag{9.4}$$

It should be noted that Eq. (9.4) satisfies the Poisson equation for individual ionic species because their total charges are conserved

$$\int_{-\infty}^{\infty} dz\,\delta\bar{\rho}_\alpha(z) = \int_{-\infty}^{\infty} dz\,\bar{\rho}_{\alpha,\text{charged}}(z) \ - \int_{-\infty}^{\infty} dz\,\bar{\rho}_{\alpha,\text{discharged}}(z) = 0 \ . \tag{9.5}$$

The results are displayed in Figures 9.5 and 9.6. For convenience, we shifted $\delta\Phi_\alpha(z)$ near the anode and cathode differently, *viz.*, $\delta\Phi_\alpha(z=-z_0) = 0$ near the anode and $\delta\Phi_\alpha(z=z_0)=0$ near the cathode. With the neglect of OH groups, the electric potential arising from the electrode charges is a linearly decreasing function of z, *i.e.*, $\Phi_{\text{electrode}}(z) = -4\pi\sigma_{\text{S}}z$. Therefore a rapid rise (drop) in $\delta\Phi_\alpha(z)$ near the anode (cathode) as z increases (decreases) from $-z_0$ (z_0) represents an efficient screening of the anode (cathode) charges by α. If we measure the contribution of species α to screening by the difference of $\delta\Phi_\alpha(z)$ at the electrode and at the screening zone

$$\begin{aligned} \delta\Delta\Phi_\alpha^{\text{SZ}} &\equiv \delta\Phi_\alpha(z=z_{\text{SZ}}^{(+)}) - \delta\Phi_\alpha(z=-z_0) \quad \text{(anode)} \ ; \\ &\equiv \delta\Phi_\alpha(z=z_0) - \delta\Phi_\alpha(z=z_{\text{SZ}}^{(-)}) \quad \text{(cathode)} \ , \end{aligned} \tag{9.6}$$

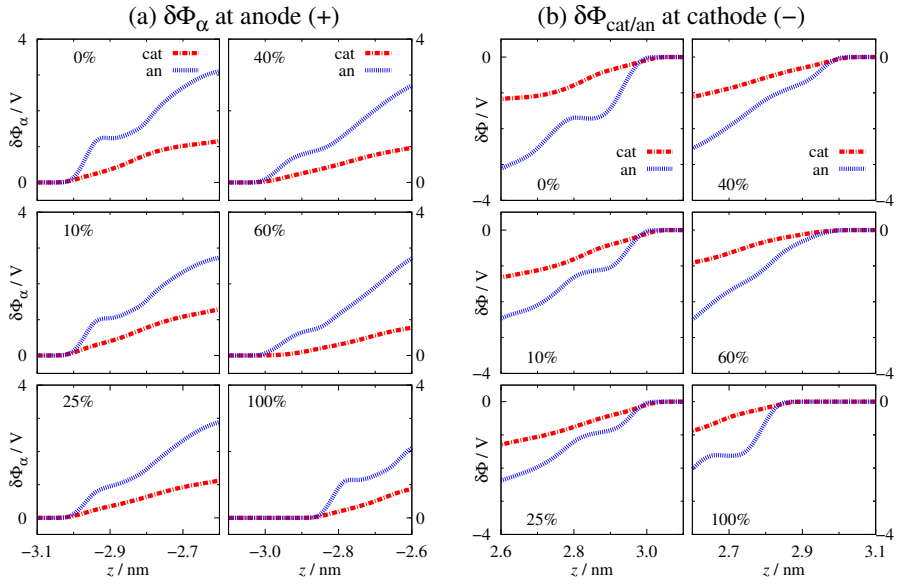

Figure 9.5: Profiles of electric potential due to each species of electrolyte near the anode (a) and near the cathode (b) in the IL supercapacitors. At the cathode with intermediate oxidation the same charge ion, anion, screens better than the opposite charge ion, cation.

the behavior of $\delta\Delta\Phi_{\alpha}^{\mathrm{SZ}}$ as the electrode oxidation changes closely mirrors that of $\delta N_{\mathrm{SZ}}^{\alpha}$ for both the IL and OE supercapacitors. (see Figures 9.7 and 9.8) Furthermore, the ratio of $\delta\Delta\Phi_{\mathrm{cation}}^{\mathrm{SZ}}$ and $\delta\Delta\Phi_{\mathrm{anion}}^{\mathrm{SZ}}$ is quite similar to that of $\delta N_{\mathrm{SZ}}^{\mathrm{cation}}$ and $\delta N_{\mathrm{SZ}}^{\mathrm{anion}}$, irrespective of the electrode oxidation. This indicates that the ion number change of SZ analyzed above provides a simple but reliable measure to quantitate the screening efficiency of ions.

With this in mind, we first consider the results for the IL supercapacitor

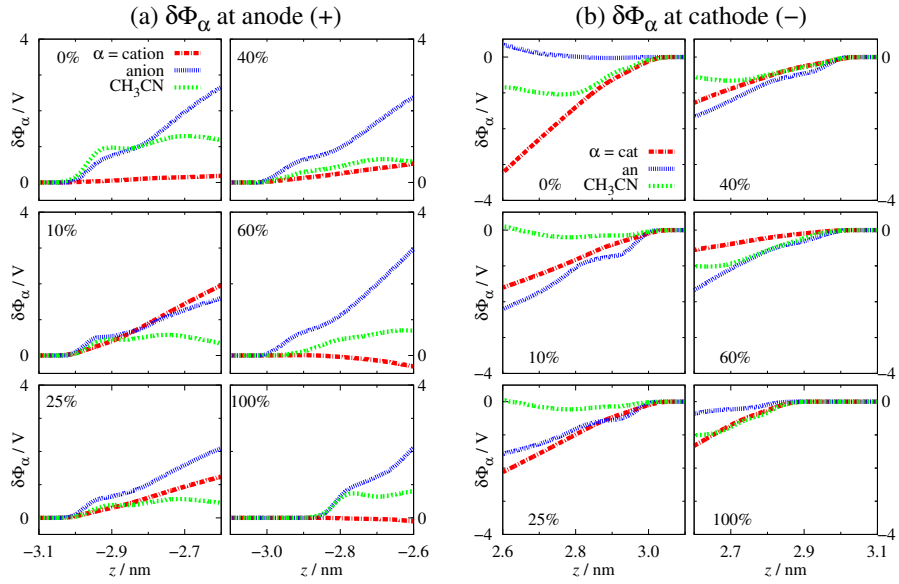

Figure 9.6: Profiles of electric potential due to each species of electrolyte near the anode (a) and near the cathode (b) in the OE supercapacitors. At the cathode the same charge ion, anion, screens better than the opposite charge ion, cation except at the neat graphene electrode (0%).

in Figure 9.5. Regardless of the electrode oxidation level, $\delta\Phi_\alpha(z)$ of the anion shows a more rapid rise near the anode and a more rapid drop near the cathode than that of the cation. This shows clearly that for the IL supercapacitor, the anions screen electrode charges better than the cations whether it is the anode or the cathode.[57] We also notice that $\delta\Delta\Phi^{\mathrm{SZ}}_{\mathrm{anion}}$ at the cathode changes significantly from $\sim$ 2.5 to $\sim$ 2.1 V as the electrode oxidation increases from 0 % to 10 %. This confirms that the rapid change

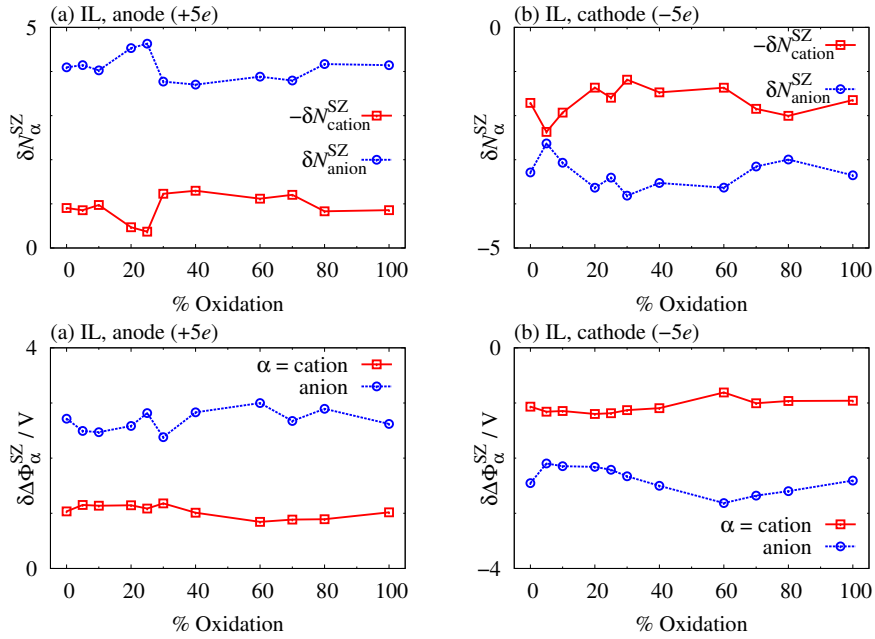

Figure 9.7: $-\delta N^{SZ}_{cation}$ and δN^{SZ}_{anion}, at the anode (a) and at the cathode (b) of the IL supercapacitor, respectively corresponding to the screening potential, $\delta\Delta\Phi^{SZ}_{cation}$ and $\delta\Delta\Phi^{SZ}_{anion}$ at the anode (c) and at the cathode (d). δN^{SZ}_{anion} and $\delta\Delta\Phi^{SZ}_{anion}$ show very similar behavior with respect to the oxidation, but those of the cation show less similar than the anion.

in the cathode potential from 0 to $\sim$ 10 % oxidation arises primarily from the anion reorganization, *i.e.*, its vacating the SZ, in the IL supercapacitor.

Variations of $\delta\Phi_\alpha(z)$ with electrode oxidation for the OE supercapacitor in Figure 9.6 are more complicated than the IL supercapacitor. Nonetheless, the trends of $\delta\Phi_\alpha(z)$ variations, e.g., total dominance of cations in cathode screening at 0 % and high oxidation, closely mirror those of δN^{SZ}_{cation} and

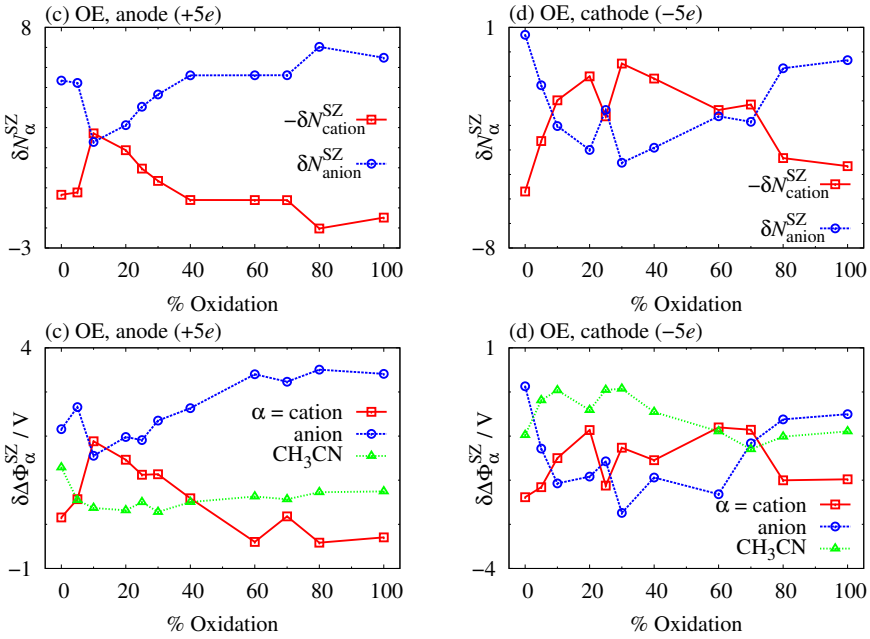

Figure 9.8: $-\delta N^{\mathrm{SZ}}_{\mathrm{cation}}$ and $\delta N^{\mathrm{SZ}}_{\mathrm{anion}}$, at the anode (a) and at the cathode (b) of the OE supercapacitor, respectively corresponding to the screening potential, $\delta\Delta\Phi^{\mathrm{SZ}}_{\mathrm{cation}}$ and $\delta\Delta\Phi^{\mathrm{SZ}}_{\mathrm{anion}}$ at the anode (c) and at the cathode (d). $|\delta N^{\mathrm{SZ}}|$ of the anion and the cation shows very similar behavior to $\delta\Delta\Phi^{\mathrm{SZ}}$ with respect to the oxidation. It is notable that for IL capacitor (Figure 9.7) $-\delta N^{\mathrm{SZ}}_{\mathrm{cation}}$ and $\delta\Delta\Phi^{\mathrm{SZ}}_{\mathrm{cation}}$ does not show as strong correspondence as those of the anion. $\delta\Delta\Phi^{\mathrm{SZ}}$ in the OE supercapacitor depends on δN^{SZ} more strongly than in the IL supercapacitor

$\delta N^{\mathrm{SZ}}_{\mathrm{anion}}$. This demonstrates that ion number changes in SZ, $\delta N^{\mathrm{SZ}}_{\alpha}$, provide a simple but reliable measure to characterize the screening efficiency of ions. One counter-intuitive aspect is that though small, co-ions make a negative

contribution to electrode screening in some cases, viz., cathode at 0 % and anode at 60 and 100 % oxidation. A small increase in the co-ion population in SZ, induced by large enhancement of the counter-ion population upon electrode charging, is responsible for this behavior (cf. Figure 9.4c and 9.4d).

Now, we apply the direct screening potential to the asymmetric potential at both electrodes shown in Figures 9.2c and 9.2d. We ascribe the similar trend in $\delta\Delta\Phi^{\text{anode}}$ of both supercapacitors to having the same main screening species, anion. Its monotonic increase with oxidation is induced by increasing hydroxyl groups, which hinders ions from reorganize and widens the screening zone. The difference between both supercapacitors are due to the cathode. At 0% oxidation, the IL supercapacitor shows a better screening ability than the OE because the former has the cation while the latter the anion as their major screening species. At the intermediate oxidation, 5 – 60%, both show the similar trends as having the same major species, anion. The cation has diffuse partial charges and bulky structure, and the anion has more concentrated partial charges and compact structure (see Figure 8.1). As suggested in previous studies,[91,98–100,135] we again ascribe the difference to the molecular geometry and the packing ability, but we apply it to the potential difference with charging, not to the charged electrode only. It is notable that this simple explanation can still be employed to the EDLC systems with more complex GO electrodes.

Finally, we make a brief contact with experiments. While several measurements[61–67] indicate that oxygen-containing functional groups in GO reduce capacitance in accord with our results, some others suggest the opposite.[59,60,113,114] One possible explanation for this disagreement is rough structure of multi-layered GO, in which ions can be intercalated. According

to several MD studies, confinement of ions in microporous environments can enhance the capacitance.[104,106,137–139] Pseudo-capacitance is another possibility, especially in the case of aqueous electrolytes.[59] For electrode screening by co-ions, our results are in good agreement with a recent experimental finding that anions can desorb from the cathode upon charging.[136]

Chapter 10

Conclusions

We studied the electric double layer capacitor composed of graphene oxide electrodes in the parallel plate configuration with pure IL electrolyte and organic electrolyte of IL via molecular dynamics simulation. The area-specific capacitance of the OE supercapacitor does not vary considerably with the oxidation of the GO electrodes until intermediate oxidation, but it monotonically decreases as the oxidation further increases. The difference between the IL supercapacitor and the OE supercapacitor is the most noticeable at lowest oxidation of GO, 0%, where the capacitance of the latter is 20% lower than that of the former, and it is dominated by the cathode capacitance.

Interestingly, BF_4^-, the counterion, is the key species in screening ability at the cathode of oxidized electrodes in both IL and OE supercapacitors, and hydrogen bonding induces this unexpected result. For the OE supercapacitor, BF_4^- ions play an important role in screening cathode charges except at very low or high oxidation. Their population enhancement through hydrogen-bond formation with GO hydroxyl groups, compared to

pure graphene or fully oxidized GO, enables BF_4^- ions to screen negative cathode charges by leaving SZ in response to charging. By contrast, at 0 % and 80–100 % oxidation, EMI^+ ions play a central role by moving into SZ of the cathode upon charging; anions are largely unavailable for screening because of their very low population in SZ prior to charging. This oxidation-dependent screening mechanism at the cathode is the main difference from the IL supercapacitor, for which BF_4^- ions are the main contributor to cathode charge screening in the entire oxidation range. For anode charge screening, counter-ions BF_4^- ions play a major role for both IL and OE supercapacitors (with the exception of the OE supercapacitor at 10 % oxidation). By replacing hydroxyl groups with epoxide groups, having less capability of hydrogen bonding, the capacitance in the OE supercapacitors are expected to show significantly less capacitance than the IL supercapacitors.[116–118]

Our results indicate that BF_4^- show a better screening efficiency than EMI^+ probably because BF_4^- are more compact and symmetric in molecular shape and charge distribution. The ability of ions to interact with GO electrodes through, e.g., hydrogen-bonding, also plays an important role, especially in OE. This opens up the possibility of optimizing screening of the cathode and anode charges separately via differing functionalizations of electrode materials and/or by using mixture electrolytes.

Appendix

Appendix A

Supplementary materials for rotational diffusion calculation in Part I

A.1 Method of $\Delta\phi(t', t'')$ calculation

The angular displacement of j-th cation from $t = t'$ to t'' is calculated with

$$\Delta\phi_j(t', t'') = \int_{t'}^{t''} dt\omega_j(t) = \sum_{k=0}^{n-1} \delta t\omega_j(t' + k\delta t), \tag{A.1}$$

where

$$\omega_j(t) = \frac{\mathbf{r}_j^{(\mathrm{rel})}(t) \times \mathbf{v}_j^{(\mathrm{rel})}(t)}{d_j^2} \tag{A.2}$$

is the instantaneous angular velocity of the j-th cation, and $t'' - t' = n\delta t$, and $\mathbf{r}_j^{(\mathrm{rel})}(t)$ and $\mathbf{v}_j^{(\mathrm{rel})}(t)$ are the position and the velocity of the reduced mass of the j-th cation at time t, and d_j is its bond length.

For calculating the MSAD, we made a trajectory saved every time step, $dt = 0.0004$ or 2 fs, the time step for MD integrator, thus the shortest time interval, but at low temperatures we took longer time intervals, δt, for the $\Delta\phi$ integration, for example, we used 100 fs for δt at $T = 0.29$ UCM.

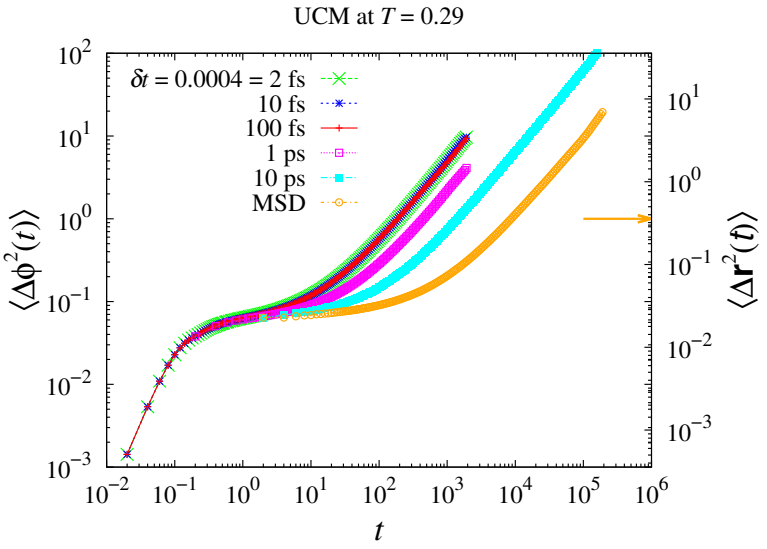

Figure A.1: MSAD of UCM at $T = 0.29$. $\delta t = 2$ fs, 10 fs, 100 fs, 1 ps, and 10 ps (from left to right increasing δt). The first thee curves collapse. For comparison the MSD of translational motion is plotted with the orange curve.

With longer δt ($> dt = 2$ fs), we used the alternate equation,

$$\Delta\phi_j(t', t'') = \sum_{k=0}^{n-1} \delta t \overline{\omega}_j(t' + k\delta t), \tag{A.3}$$

where

$$\overline{\omega}_j(t) = \frac{\hat{\mathbf{u}}_j(t) \times \hat{\mathbf{u}}_j(t + \delta t)}{\delta t} \tag{A.4}$$

is the average angular velocity during δt, where $\hat{u}_j(t)$ is the orientational vector of the $j-$th cation at time t. With $\delta t = dt$, the Eq. (A.4) becomes

Eq. (A.2), and the two Eqs. are equivalent.

A.2 Dependence of the time interval on $\Delta\phi(t', t'')$

Figure A.1 is the plot of MSAD of UCM at $T = 0.29$ with $\delta t = 2$ fs (green), 10 fs (blue), 100 fs (red), 1 ps (magenta), and 10 ps (cyan), and the three shortest δt cases overlap with each other. With the longer δt (≥ 1 ps) the MSAD shows longer subdiffusive regime. The stacking of small angular displacements in librational motion contributes less with the longer δt, and it takes more time for it to reach diffusive regime.

We used the MSAD results with $\delta t = 100$ fs at the lowest temperature for all the systems in this study. Although D_{R} is estimated smaller with longer δt, the MSAD results with $\delta t \leq 100$fs are believed to be reliable.

The DSE relations in our systems break down much more severely than the breakdown of the SE relation at low temperatures (see Figure 5.7). Because τ_{R} is calculated correctly, we suspect that D_{R} is calculated much greater than expected from the DSE relation, compared to the amount of decoupling in translational SE relation. We would have obtained less severe decoupling of DSE relation with less D_{R} if we had used coarser time intervals, $\delta t \geq 1$ ps, of integration.

With the finest δt at all temperatures, however, we would not obtain less severe decoupling of DSE relation than shown in Figure 5.7 because D_{R} tends to have greater value with shorter δt, and MSAD converges at $\delta t = 100$ fs, which is the longest time interval for integration in our study. Therefore, the interestingly severe decoupling of DSE relation is thus technically quite

a reliable result. The physics underneath it, however, is yet to be looked into more deeply.

We believe that diffusion in both translation and rotation occurs with occasional jumps, or excitations. Refs. [8,42] manifested this phenomenon in translational motion of spin models and an atomistic model. Because we can observe the subdiffusive behavior even with the finest time interval, $\delta t =$ 2fs, in Figure A.1, we also expect that the angular jumps can be observed in $\Delta\phi$, but rather continuous, not as abrupt as the translational ones.

Concerning the angular jumps, longer time interval, $\delta t \geq$1ps, would make them to seem abrupt. A proper coarse-graining in time scale could be one way of circumventing this breakdown, but we are not sure if it will be proper or just arbitrary a coarse-graining. We are planning to study on this. Moreover, as we indicated in Part I, because there is no other way, at the present, of calculating angular displacement unboundedly, we adopted this definition for angular displacement.

Appendix B

Supplementary materials for Part II

B.1 Screening zone in the supercapacitors

We introduce the number of ions (or molecules) contained inside the electrolyte volume from the electrode to position z as

$$N_{\alpha,\sigma}(z) \equiv A_0 \int_{-z_0}^{z} dz' \, \bar{n}_{\alpha,\sigma}(z') \quad \text{(anode)}; \tag{B.1}$$

$$\equiv A_0 \int_{z}^{z_0} dz' \, \bar{n}_{\alpha,\sigma}(z') \quad \text{(cathode)}, \tag{B.2}$$

where $\bar{n}_{\alpha,\sigma}(z')$ is the number density of species α (= cation or anion) at z' averaged over x and y, σ denotes the charge state of the electrode (charged or discharged) and $A_0 = 4x_0y_0$ is the electrode surface area (see Figures B.3 and B.4). The center-of-mass position is employed to describe the locations of α. The change in $N_\alpha(z)$ with charging is defined by $\delta N_\alpha(z) \equiv N_{\alpha,\mathrm{charged}}(z) - N_{\alpha,\mathrm{discharged}}(z)$. The number difference of the counter-ions

and co-ions is

$$\delta\Delta N^{(\text{anode})}_{\text{excess}}(z) = \delta N_{\text{anion}}(z) - \delta N_{\text{cation}}(z) \quad \text{(anode)}; \tag{B.3}$$

$$\delta\Delta N^{(\text{cathode})}_{\text{excess}}(z) = \delta N_{\text{cation}}(z) - \delta N_{\text{anion}}(z) \quad \text{(cathode)}, \tag{B.4}$$

The screening zone, SZ, of a charged electrode is defined as the electrolyte volume of $z < z^{(+)}_{\text{SZ}}$ at the anode and $z > z^{(-)}_{\text{SZ}}$ at the cathode, such that

$$N_0 = \delta\Delta N^{\text{SZ}}_{\text{excess}} = \delta\Delta N^{(\text{anode})}_{\text{excess}}(z^{(+)}_{\text{SZ}}) \quad \text{(anode)} \; ; \tag{B.5}$$

$$= \delta\Delta N^{(\text{cathode})}_{\text{excess}}(z^{(-)}_{\text{SZ}}) \quad \text{(cathode)} \; , \tag{B.6}$$

where N_0 is the magnitude of the total charge of the charged electrode in units of e. Thus the total charge of the charged electrode and its screening zone is 0. For simplicity, we use $N^{\text{SZ}}_{\alpha,\sigma}$ to denote the number of ions or molecules of species α in the SZ ($N^{\text{SZ}}_{\alpha,\sigma} \equiv N_{\alpha,\sigma}(z_{\text{SZ}})$), and $\delta N^{\text{SZ}}_{\alpha}$ its change with electrode charging ($\delta N^{\text{SZ}}_{\alpha} = N^{\text{SZ}}_{\alpha,\text{charged}} - N^{\text{SZ}}_{\alpha,\text{discharged}}$) (see Figures 9.3 and 9.4). We can measure the contribution of species α to screening by the difference of $\delta\Phi_\alpha(z)$ at the electrode and at $z^{(\pm)}_{\text{SZ}}$

$$\begin{aligned} \delta\Delta\Phi^{\text{SZ}}_{\alpha} &\equiv \delta\Phi_\alpha(z = z^{(+)}_{\text{SZ}}) - \delta\Phi_\alpha(z = -z_0) \quad \text{(anode)} \; ; \\ &\equiv \delta\Phi_\alpha(z = z_0) - \delta\Phi_\alpha(z = z^{(-)}_{\text{SZ}}) \quad \text{(cathode)} \; . \end{aligned} \tag{B.7}$$

Here $\delta\Phi_\alpha(z)$ (Eq. (9.4)) is the change in electric potential at z associated with reorganization of species α in response to electrode charging.

MD results for $\delta\Delta N^{\alpha}_{\text{excess}}(z)$ in the IL supercapacitor with $N_0 = 5$ are shown in Figure B.1. Intersections of $\delta\Delta N^{\alpha}_{\text{excess}}(z)$ curves and the $N_0 = 5$ horizontal line (dotted red line) satisfy Eqs. (B.3) and (B.4). We note that

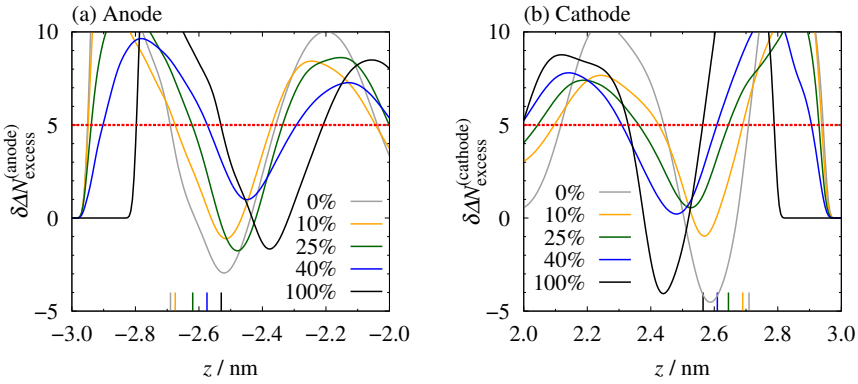

Figure B.1: Profiles of (a) $\delta\Delta N_{\text{excess}}^{(\text{anode})}(z)$ and (b) $\delta\Delta N_{\text{excess}}^{(\text{cathode})}(z)$ in the IL supercapacitors with $N_0 = 5$ at selected oxidations. The locations z_{SZ} are marked as short vertical lines on the x-axis and compiled in Table B.1.

there are multiple intersections. This is due to alternating distributions of cations and anions near the charged electrodes.[57] Among these, we choose the smallest volume of the electrolyte that contains both counter-ions and co-ions as SZ. Our MD results indicate that electric potential, though oscillatory, changes little beyond the SZ thus determined. We notice that SZ generally increases as electrode oxidation increases (Figure B.1 and Table B.1). This points to decreasing screening efficiency of electrolytes with increasing electrode oxidation.

Table B.1: The range of the screening zone of each oxidation, z^{SZ}.¶

	IL		OE	
Oxidation	Anode	Cathode	Anode	Cathode
0%	−2.690	2.710	−2.675	2.690
5%	−2.695	2.705	−2.640	2.620
10%	−2.675	2.690	−2.615	2.630
20%	−2.660	2.650	−2.615	2.660
25%	−2.620	2.645	−2.640	2.600
30%	−2.635	2.635	−2.585	2.560
40%	−2.575	2.610	−2.560	2.535
60%	−2.550	2.575	−2.555	2.485
70%	−2.560	2.555	−2.480	2.545
80%	−2.530	2.555	−2.505	2.485
100%	−2.530	2.565	−2.480	2.500

¶Units: nm.

B.2 Number density profiles

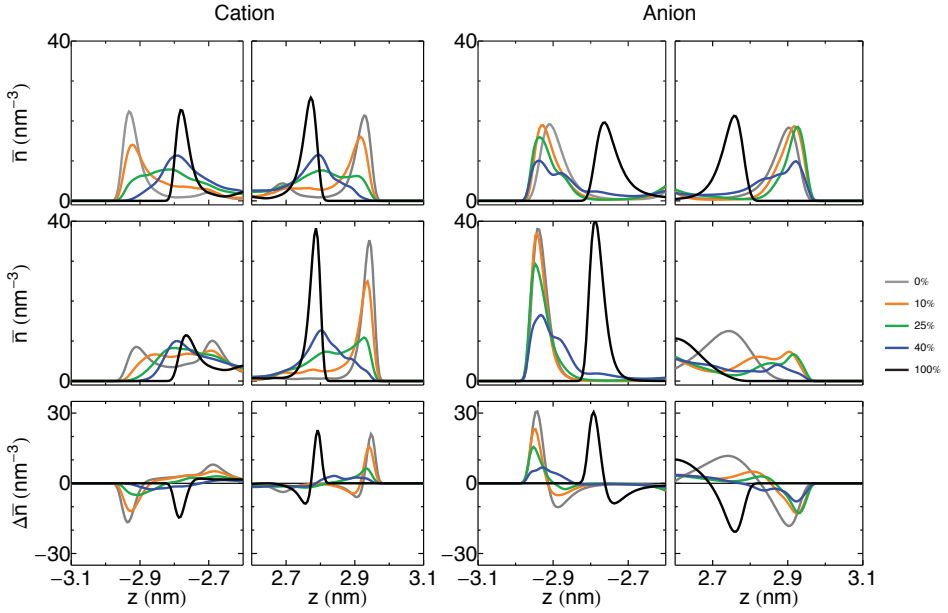

Figure B.2: Number densities in the IL supercapacitors (units: nm^{-3}, Ref. [57]). The upper and middle panels of each column show, respectively, the discharged and charged cases while their difference is shown in the lower panel.

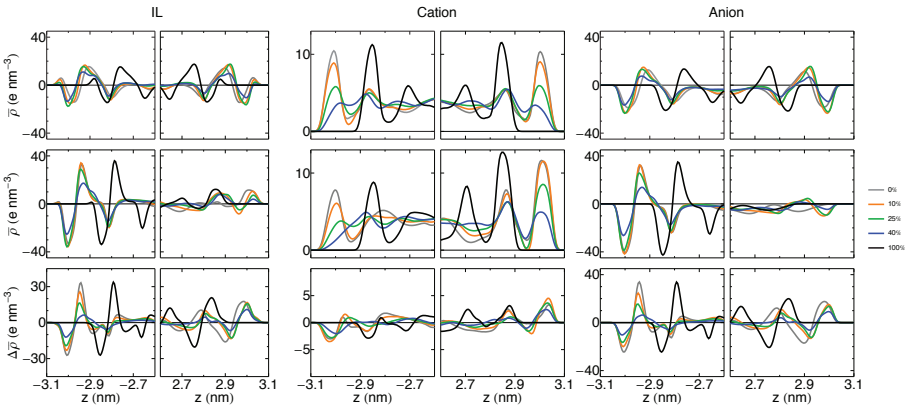

Figure B.3: Charge densities in the IL supercapacitors (units: nm^{-3}, Ref. [57]). The upper and middle panels of each column show, respectively, the discharged and charged cases while their difference is shown in the lower panel.

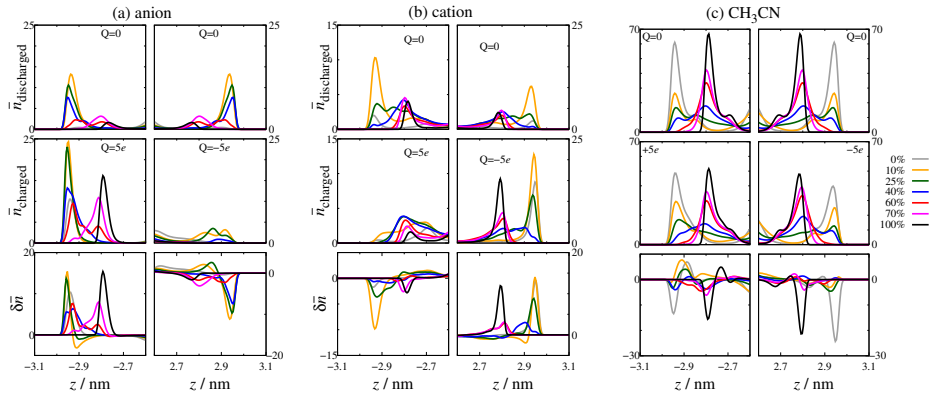

Figure B.4: Number densities of (a) anions, (b) cations and (c) acetonitrile in the OE supercapacitors (units: nm^{-3}). The center-of-mass is used to represent positions of ions and molecules.

B.3 Charge density profiles

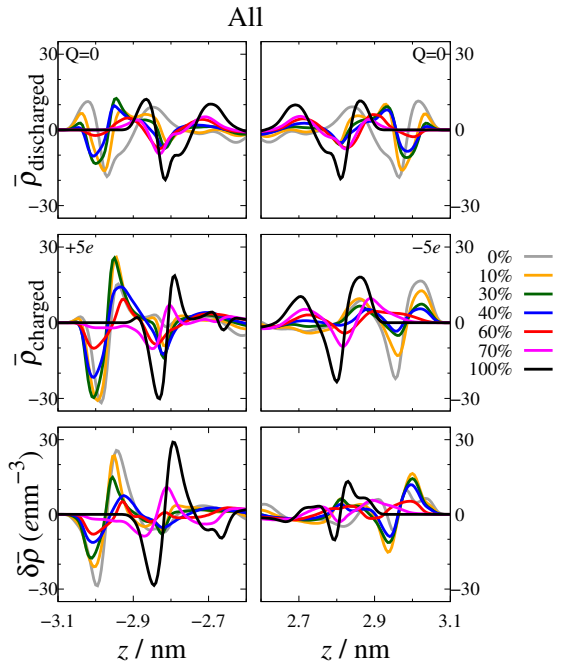

Figure B.5: Overall charge densities ($e$nm^{-3}) in the OE supercapacitors near the anode and cathode. The upper and middle panels show the discharged and charged cases, respectively, while their difference is displayed in the lower panel.

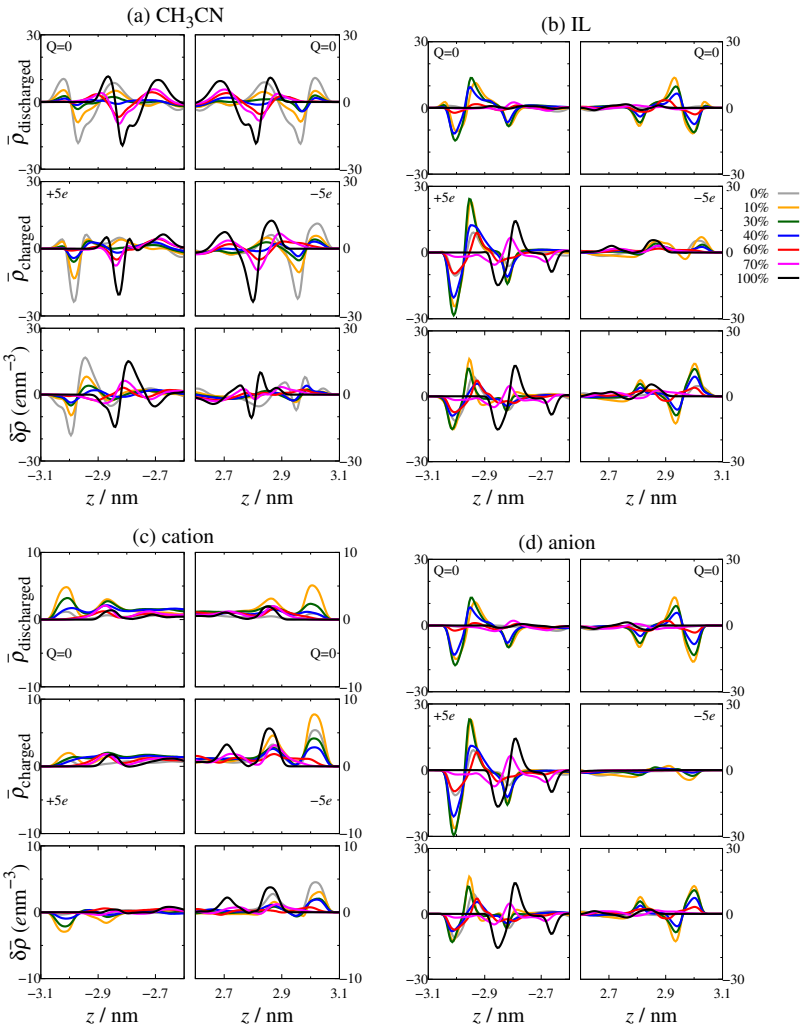

Figure B.6: Charge densities (e/nm^3) of (a) acetonitrile, (b) cations+anions, (c) cations, and (d) anions in the OE supercapacitors.

Comparison of right columns of Figure B.6b and c shows that the charge density profile of cations near cathode is quite different from that of cations and anions combined except for the 0% case. The charge density profile of anions near anode, on the other hand, is nearly the same as that of cations and anions combined (cf. left columns of Figure B.6b and d).

B.4 Orientation of molecules

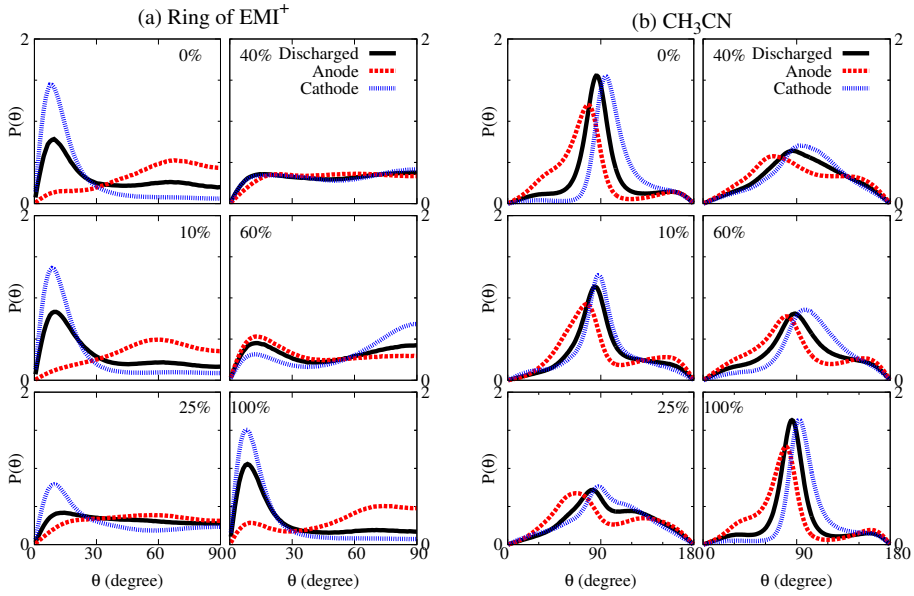

Figure B.7: Probability distribution $P(\theta)$ of (a) EMI^+ and (b) CH_3CN orientations in the first layer with the same criteria in Figures 9.3 and 9.4.

For the discharged case, we use an average value between $z_{SZ}^{(+)}$ and $z_{SZ}^{(-)}$: $\Delta z < z_{SZ}^{(\mathrm{discharged})}$, where Δz is the distance from the electrode, and $z_{SZ}^{(\mathrm{discharged})} = (-z_{SZ}^{(+)} + z_{SZ}^{(-)})/2$. $P(\theta)$ is normalized as $\int P(\theta)\, d\theta = 1$. In (a), θ is the angle between the normal to the electrode surface and the normal to the EMI^+ ring. Thus $\theta = 0^\circ$ represents the ring orientation parallel to the electrode surface. In (b), θ is defined as the angle between the normal to the electrode surface and the direction from the cyano carbon to the methyl

carbon of acetonitrile. As θ approaches 0°, acetonitrile becomes perpendicular to the electrode surface with its N atom facing the electrode. At 180°, the orientation of N is toward the bulk solvent.

B.5 Electric potential profiles

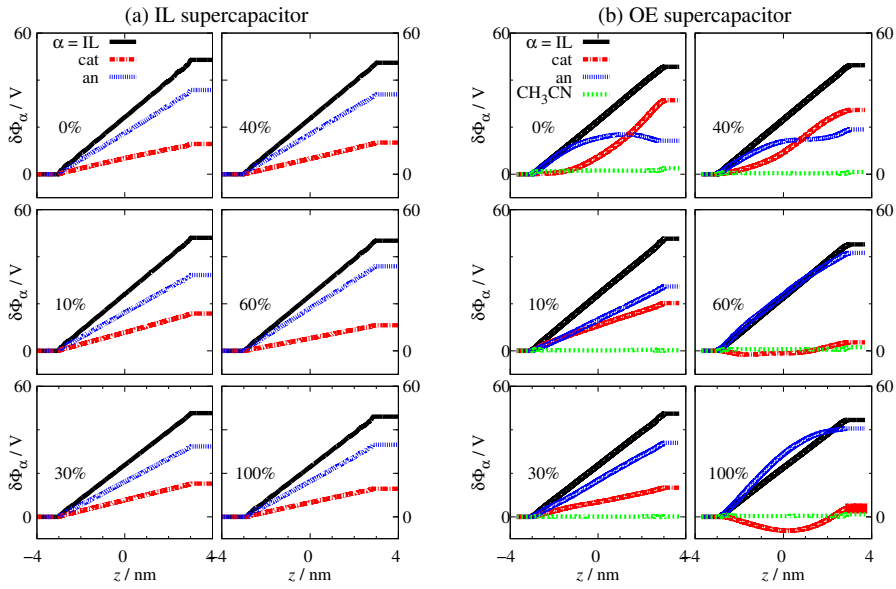

Figure B.8: MD results for $\delta\Phi_\alpha(z)$ in Eq. (9.4). In the OE capacitor in (b), $\delta\Phi_{\text{cation}}(z)$ and $\delta\Phi_{\text{anion}}(z)$ show a nonlinear behavior, especially in the region near $z = 0$, probably due to low ion concentration. The electric potential difference of the anode and the cathode due to electrode charges $\pm 5e$ ranges from ~ -51.2 V at 0% to -49.8 V at100% oxidation.

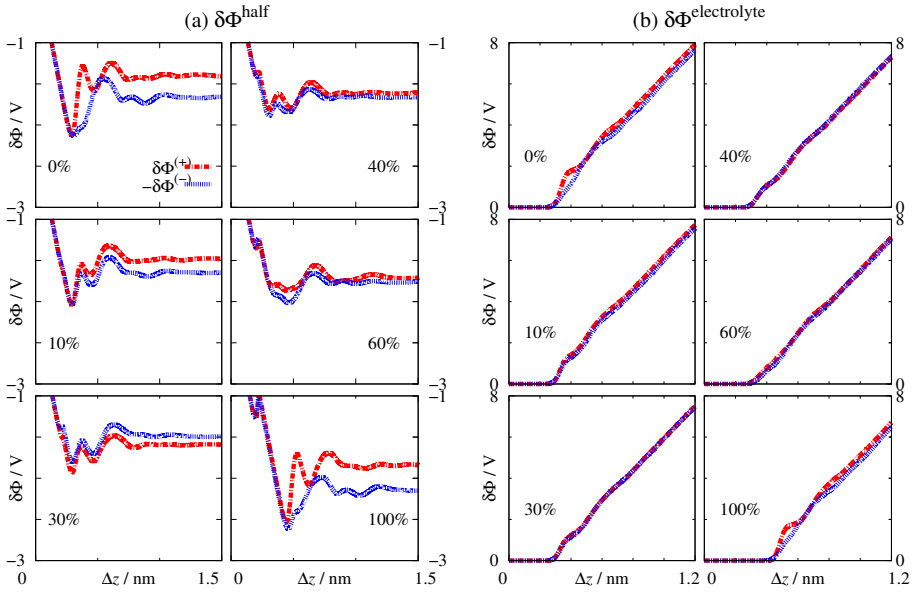

Figure B.9: (a) Profile of total electric potential near the anode (red) and cathode (blue) and (b) contribution from the electrolyte in the OE supercapacitor. $\Delta z = |z - (\pm z_0)|$ is the distance from the electrode.

Bibliography

[1] Weingärtner, H. "Understanding ionic liquids at the molecular level: facts, problems, and controversies." *Angew. Chem. Int. Ed.* **2008**, *47*, 654–670.

[2] Brennecke, J. F.; Maginn, E. J. "Ionic Liquids: Innovative Fluids for Chemical Processing." *AIChE Journal* **2001**, *47*, 2384–2389.

[3] Park, S.-W.; Kim, S.; Jung, Y. "Time scale of dynamic heterogeneity in model ionic liquids and its relation to static length scale and charge distribution." *Phys. Chem. Chem. Phys.* **2015**, *17*, 29281–29292.

[4] Kim, S.; Park, S.-W.; Jung, Y. (submitted to Phys. Chem. Chem. Phys.).

[5] Berthier, L.; Biroli, G. "Theoretical perspective on the glass transition and amorphous materials." *Rev. Mod. Phys.* **2011**, *83*, 587.

[6] Malvaldi, M.; Chiappe, C. "From molten salts to ionic liquids: effect of ion asymmetry and charge distribution." *J. Phys.: Condens. Matter* **2008**, *20*, 035108.

[7] Jeong, D.; Choi, M. Y.; Jung, Y.; Kim, H. J. "1/f spectrum and memory function analysis of solvation dynamics in a room-temperature ionic liquid." *J. Chem. Phys.* **2008**, *128*, 174504.

[8] Jeong, D.; Choi, M. Y.; Kim, H. J.; Jung, Y. "Fragility, Stokes-Einstein violation, and correlated local excitations in a coarse-grained model of an ionic liquid." *Phys. Chem. Chem. Phys.* **2010**, *12*, 2001–2010.

[9] Shim, Y.; Duan, J.; Choi, M. Y.; Kim, H. J. "Solvation in molecular ionic liquids." *J. Chem. Phys.* **2003**, *119*, 6411.

[10] Shim, Y.; Kim, H. J. "Dielectric Relaxation, Ion Conductivity, Solvent Rotation, and Solvation Dynamics in a Room-Temperature Ionic Liquid." *J. Phys. Chem. B* **2008**, *112*, 11028–11038.

[11] Jeong, D.; Kim, D.; Choi, M. Y.; Kim, H. J.; Jung, Y. In *Ionic Liquids: Theory, Properties, New Approaches*; Kokorin, A., Ed.; InTech, 2011; Chapter 7, pp 167–182.

[12] Kim, D.; Jeong, D.; Jung, Y. "Dynamic propensity as an indicator of heterogeneity in room-temperature ionic liquids." *Phys. Chem. Chem. Phys.* **2014**, *16*, 19712–19719.

[13] Roy, D.; Patel, N.; Conte, S.; Maroncelli, M. "Dynamics in an Idealized Ionic Liquid Model." *J. Phys. Chem. B* **2010**, *114*, 8410–8424.

[14] Roy, D.; Maroncelli, M. "An Improved Four-Site Ionic Liquid Model." *J. Phys. Chem. B* **2010**, *114*, 12629–12631.

[15] Margulis, C. J.; Stern, H. A.; Berne, B. J. "Computer Simulation of a "Green Chemistry" Room-Temperature Ionic Solvent." *J. Phys. Chem. B* **2002**, *106*, 12017–12021.

[16] Pópolo, M. G. D.; Voth, G. A. "On the structure and dynamics of ionic liquids." *J. Phys. Chem. B* **2004**, *108*, 1744–1752.

[17] Hu, Z.; Margulis, C. J. "Heterogeneity in a room-temperature ionic liquid: Persistent local environments and the red-edge effect." *Proc. Natl. Acad. Sci. U.S.A.* **2006**, *103*, 831–836.

[18] Habasaki, J.; Ngai, K. L. "Heterogeneous dynamics of ionic liquids from molecular dynamics simulations." *J. Chem. Phys.* **2008**, *129*, 194501.

[19] Pal, T.; Biswas, R. "Slow solvation in ionic liquids: Connections to non-Gaussian moves and multi-point correlations." *J. Chem. Phys.* **2014**, *141*, 104501.

[20] Flenner, E.; Szamel, G. "Dynamic heterogeneity in a glass forming fluid: susceptibility, structure factor, and correlation length." *Phys. Rev. Lett.* **2010**, *105*, 217801.

[21] Flenner, E.; Szamel, G. "Characterizing dynamic length scales in glass-forming liquids." *Nature Phys.* **2012**, *8*, 696–697.

[22] Glotzer, S. C.; Novikov, V. N.; Schrøder, T. B. "Time-dependent, four-point density correlation function description of dynamical heterogeneity and decoupling in supercooled liquids." *J. Chem. Phys.* **2000**, *112*, 509–512.

[23] Lacevic, N.; Starr, F.; Schroder, T.; Glotzer, S. "Spatially heterogeneous dynamics investigated via a time-dependent four-point density correlation function." *J. Chem. Phys.* **2003**, *119*, 7372–7387.

[24] Kim, K.; Saito, S. "Multiple length and time scales of dynamic heterogeneities in model glass-forming liquids: A systematic analysis of multi-point and multi-time correlations." *J. Chem. Phys.* **2013**, *138*, 12A506.

[25] Mizuno, H.; Yamamoto, R. "Dynamical heterogeneity in a highly supercooled liquid: Consistent calculations of correlation length, intensity, and lifetime." *Phys. Rev. E* **2011**, *84*, 011506.

[26] Flenner, E.; Szamel, G. "Lifetime of dynamic heterogeneities in a binary Lennard-Jones mixture." *Phys. Rev. E* **2004**, *70*, 052501.

[27] Kim, K.; Saito, S. "Multiple time scales hidden in heterogeneous dynamics of glass-forming liquids." *Phys. Rev. E* **2009**, *79*, 060501.

[28] Kim, K.; Saito, S. "Multi-time density correlation functions in glass-forming liquids: Probing dynamical heterogeneity and its lifetime." *J. Chem. Phys.* **2010**, *133*, 044511.

[29] Cicerone, M. T.; Ediger, M. D. "Relaxation of spatially heterogeneous dynamic domains in supercooled orthoterphenyl." *J. Chem. Phys.* **1995**, *103*, 5684.

[30] Wang, C.-Y.; Ediger, M. D. "How long do regions of different dynamics persist in supercooled o-terphenyl?" *J. Phys. Chem. B* **1999**, *103*, 4177–4184.

[31] Ediger, M. D. "Spatially heterogeneous dynamics in supercooled liquids." *Annu. Rev. Phys. Chem.* **2000**, *51*, 99–128.

[32] Léonard, S.; Berthier, L. "Lifetime of dynamic heterogeneity in strong and fragile kinetically constrained spin models." *J. Phys.: Condens. Matter* **2005**, *17*, S3571–S3577.

[33] Mizuno, H.; Yamamoto, R. "Lifetime of dynamical heterogeneity in a highly supercooled liquid." *Phys. Rev. E* **2010**, *82*, 030501(R).

[34] Jung, Y.; Garrahan, J. P.; Chandler, D. "Dynamical exchanges in facilitated models of supercooled liquids." *J. Chem. Phys.* **2005**, *123*, 084509.

[35] Choi, S.-W.; Kim, S.; Jung, Y. "Dynamic heterogeneity in crossover spin facilitated model of supercooled liquid and fractional Stokes-Einstein relation." *J. Chem. Phys.* **2015**, *142*, 244506.

[36] Berthier, L.; Jack, R. L. "Structure and dynamics of glass formers: Predictability at large length scales." *Phys. Rev. E* **2007**, *76*, 041509.

[37] Dasgupta, C.; Indrani, A. V.; Ramaswamy, S.; Phani, M. K. "Is There a Growing Correlation Length near the Glass Transition?" *Europhys. Lett.* **1991**, *15*, 307.

[38] Mackowiak, S. A.; Leone, L. M.; Kaufman, L. J. "Probe dependence of spatially heterogeneous dynamics in supercooled glycerol as revealed by single molecule microscopy." *Phys. Chem. Chem. Phys.* **2011**, *13*, 1786–1799.

[39] Karmakar, S.; Dasgupta, C.; Sastry, S. "Growing length and time scales in glass-forming liquids." *Proc. Natl. Acad. Sci. U.S.A.* **2009**, *106*, 3675–3679.

[40] Szamel, G.; Flenner, E. "Four-point susceptibility of a glass-forming binary mixture: Brownian dynamics." *Phys. Rev. E* **2006**, *74*, 021507.

[41] Szamel, G.; Flenner, E. "Diverging length scale of the inhomogeneous mode-coupling theory: A numerical investigation." *Phys. Rev. E* **2010**, *81*, 031507.

[42] Jung, Y.; Garrahan, J. P.; Chandler, D. "Excitation lines and the breakdown of Stokes-Einstein relations in supercooled liquids." *Phys. Rev. E* **2004**, *69*, 061205.

[43] Kämmerer, S.; Kob, W.; Schilling, R. "Dynamics of the rotational degrees of freedom in a supercooled liquid of diatomic molecules." *Phys. Rev. E* **1997**, *56*, 5450–5461.

[44] Chong, S.-H.; Kob, W. "Coupling and Decoupling between Translational and Rotational Dynamics in a Supercooled Molecular Liquid." *Phys. Rev. Lett.* **2009**, *102*, 025702.

[45] Mazza, M. G.; Giovambattista, N.; Stanley, H. E.; Starr, F. W. "Connection of translational and rotational dynamical heterogeneities with the breakdown of the Stokes-Einstein and Stokes-Einstein-Debye relations in water." *Phys. Rev. E* **2007**, *76*, 031203.

[46] Cicerone, M. T.; Ediger, M. D. "Enhanced translation of probe

molecules in supercooled o-terphenyl: Signature of spatially heterogeneous dynamics?" *J. Chem. Phys.* **1996**, *104*, 7210.

[47] Hedges, L. O.; Maibaum, L.; Chandler, D.; Garrahan, J. P. "Decoupling of exchange and persistence times in atomistic models of glass formers." *J. Chem. Phys.* **2007**, *127*, 211101.

[48] Doliwa, B.; Heuer, A. "Cage effect, local anisotropies, and dynamic heterogeneities at the glass transition: A computer study of hard spheres." *Phys. Rev. Lett.* **1998**, *80*, 4915–4918.

[49] Qian, J.; Hentschke, R.; Heuer, A. "Dynamic heterogeneities of translational and rotational motion of a molecular glass former from computer simulations." *J. Chem. Phys.* **1999**, *110*, 4514–4522.

[50] Schmidt-Rohr, K.; Spiess, H. W. "Nature of nonexponential loss of correlation above the glass transition investigated by multidimensional NMR." *Phys. Rev. Lett.* **1991**, *66*, 3020–3023.

[51] Heuer, A.; Wilhelm, M.; Zimmermann, H.; Spiess, H. W. "Rate Memory of Structural Relaxation in Glasses and Its Detection by Multidimensional Nmr." *Phys. Rev. Lett.* **1995**, *75*, 2851–2854.

[52] Heuer, A. "Information content of multitime correlation functions for the interpretation of structural relaxation in glass-forming systems." *Phys. Rev. E* **1997**, *56*, 730.

[53] Heuer, A.; Okun, K. "Heterogeneous and homogeneous dynamics in a simulated polymer melt: Analysis of multi-time correlation functions." *J. Chem. Phys.* **1997**, *106*, 6176.

[54] Yamamoto, R.; Onuki, A. "Dynamics of highly supercooled liquids: Heterogeneity, rheology, and diffusion." *Phys. Rev. E* **1998**, *58*, 3515.

[55] Kim, J.; Kim, C.; Sung, B. J. "Simulation Study of Seemingly Fickian but Heterogeneous Dynamics of Two Dimensional Colloids." *Phys. Rev. Lett.* **2013**, *110*, 047801.

[56] Edmond, K. V.; Elsesser, M. T.; Hunter, G. L.; Pine, D. J.; Weeks, E. R. "Decoupling of rotational and translational diffusion in supercooled colloidal fluids." *Proc. Natl. Acad. Sci. U.S.A.* **2012**, *109*, 17891–17896.

[57] DeYoung, A. D.; Park, S.-W.; Dhumal, N. R.; Shim, Y.; Jung, Y.; Kim, H. J. "Graphene Oxide Supercapacitors: A Computer Simulation Study." *J. Phys. Chem. C* **2014**, *118*, 18472–18480.

[58] Park, S.-W.; DeYoung, A. D.; Dhumal, N. R.; Shim, Y.; Jung, Y.; Kim, H. J. (in preparation).

[59] Xu, B.; Yue, S.; Sui, Z.; Zhang, X.; Hou, S.; Cao, G.; Yang, Y. "What is the Choice for Supercapacitors: Graphene or Graphene Oxide?" *Energy Environ. Sci.* **2011**, *4*, 2826–2830.

[60] Zhao, B.; Liu, P.; Jiang, Y.; Pan, D.; Tao, H.; Song, J.; Fang, T.; Xu, W. "Supercapacitor Performances of Thermally Reduced Graphene Oxide." *J. Power Sources* **2012**, *198*, 423–427.

[61] Shao, Y.; Wang, J.; Engelhard, M.; Wang, C.; Lin, Y. "Facile and Controllable Electrochemical Reduction of Graphene Oxide and Its Applications." *J. Mater. Chem.* **2010**, *20*, 743–748.

[62] Buglione, L.; Chng, E. L. K.; Ambrosi, A.; Sofer, Z.; Pumera, M. "Graphene Materials Preparation Methods Have Dramatic Influence upon Their Capacitance." *Electrochem. Commun.* **2012**, *14*, 5–8.

[63] Koinuma, M.; Tateishi, H.; Hatakeyama, K.; Miyamoto, S.; Ogata, C.; Funatsu, A.; Taniguchi, T.; Matsumoto, Y. "Analysis of Reduced Graphene Oxides by X-Ray Photoelectron Spectroscopy and Electrochemical Capacitance." *Chem. Lett.* **2013**, *42*, 924–926.

[64] Tong, H.; Zhu, J.; Chen, J.; Han, Y.; Yang, S.; Ding, B.; Zhang, X. "Electrochemical Reduction of Graphene Oxide and Its Electrochemical Capacitive Performance." *J. Solid State Electrochem.* **2013**, *17*, 2857–2863.

[65] Ciszewski, M.; Mianowski, A.; Nawrat, G. "Preparation and Electrochemical Properties of Sodium-Reduced Graphene Oxide." *J. Mater. Sci.: Mater. Electron.* **2013**, *24*, 3382–3386.

[66] Yu, H.; He, J.; Sun, L.; Tanaka, S.; Fugetsu, B. "Influence of the Electrochemical Reduction Process on the Performance of Graphene-Based Capacitors." *Carbon* **2013**, *51*, 94–101.

[67] Yang, J.; Gunasekaran, S. "Electrochemically Reduced Graphene Oxide Sheets for Use in High Performance Supercapacitors." *Carbon* **2013**, *51*, 36–44.

[68] Shirota, H.; Castner, E. W. "Physical Properties and Intermolecular Dynamics of an Ionic Liquid Compared with Its Isoelectronic Neutral Binary Solution." *J. Phys. Chem. A* **2005**, *109*, 9388–9392.

[69] Tokuda, H.; Ishii, K.; Susan, M. A. B. H.; Tsuzuki, S.; Hayamizu, K.; Watanabe, M. "Physicochemical Properties and Structures of Room-Temperature Ionic Liquids. 3. Variation of Cationic Structures." *J. Phys. Chem. B* **2006**, *110*, 2833–2839.

[70] Kobrak, M. N.; Sandalow, N. "An Electrostatic Interpretation of Structure-Property Relationships in Ionic Liquids." Molten Salts XIV. Pennington, NJ, 2006; pp 417–425.

[71] Spohr, H. V.; Patey, G. N. "Structural and dynamical properties of ionic liquids: The influence of charge location." *J. Chem. Phys.* **2009**, *130*, 104506.

[72] Triolo, A.; Russina, O.; Arrighi, V.; Juranyi, F.; Janssen, S.; Gordon, C. M. "Quasielastic neutron scattering characterization of the relaxation processes in a room temperature ionic liquid." *J. Chem. Phys.* **2003**, *119*, 8549.

[73] Chakrabarty, D.; Seth, D.; Chakraborty, A.; Sarkar, N. "Dynamics of solvation and rotational relaxation of coumarin 153 in ionic liquid confined nanometer-sized microemulsions." *J. Phys. Chem. B* **2005**, *109*, 5753–5758.

[74] Bhargava, B. L.; Balasubramanian, S. "Dynamics in a room-temperature ionic liquid: A computer simulation study of 1,3-dimethylimidazolium chloride." *J. Chem. Phys.* **2005**, *123*, 144505.

[75] Urahata, S. M.; Ribeiro, M. C. C. "Single particle dynamics in ionic liquids of 1-alkyl-3-methylimidazolium cations." *J. Chem. Phys.* **2005**, *122*, 024511.

[76] Morrow, T. I.; Maginn, E. J. "Molecular Dynamics Study of the Ionic Liquid 1- n-Butyl-3-methylimidazolium Hexafluorophosphate." *J. Phys. Chem. B* **2002**, *106*, 12807–12813.

[77] Wang, Y.; Voth, G. A. "Unique Spatial Heterogeneity in Ionic Liquids." *J. Am. Chem. Soc.* **2005**, *127*, 12192–12193.

[78] Edwards, S. F.; Anderson, P. W. "Theory of Spin Glasses." *J. Phys. F: Metal Phys.* **1975**, *5*, 965–974.

[79] Kumar, P.; Buldyrev, S. V.; Becker, S. R.; Poole, P. H.; Starr, F. W.; Stanley, H. E. "Relation between the Widom line and the breakdown of the Stokes-Einstein relation in supercooled water." *Proc. Natl. Acad. Sci. U.S.A.* **2007**, *104*, 9575–9579.

[80] Xu, L.; Mallamace, F.; Yan, Z.; Starr, F. W.; Buldyrev, S. V.; Stanley, H. E. "Appearance of a fractional Stokes-Einstein relation in water and a structural interpretation of its onset." *Nature Phys.* **2009**, *5*, 565–569.

[81] Pronk, S.; Páll, S.; Schulz, R.; Larsson, P.; Bjelkmar, P.; Apostolov, R.; Shirts, M. R.; Smith, J. C.; Kasson, P. M.; van der Spoel, D.; Hess, B.; Lindahl, E. "GROMACS 4.5: a high-throughput and highly parallel open source molecular simulation toolkit." *Bioinformatics* **2013**, *29*, 845–854.

[82] Weeks, J. D.; Chandler, D.; Andersen, H. C. "Role of Repulsive Forces in Determining the Equilibrium Structure of Simple Liquids." *J. Chem. Phys.* **1971**, *54*, 5237.

[83] Canongia Lopes, J. N.; Deschamps, J.; Pádua, A. A. H. "Modeling Ionic Liquids Using a Systematic All-Atom Force Field." *J. Phys. Chem. B* **2004**, *108*, 2038–2047.

[84] Mitsuhiro, K.; Harris, K. R.; Tsuchihashi, N.; Ibuki, K.; Ueno, M. "Effect of Pressure on Transport Properties of the Ionic Liquid 1-Butyl-3-methylimidazolium Hexafluorophosphate." *J. Phys. Chem. B* **2007**, *111*, 2062–2069.

[85] Kob, W.; Andersen, H. C. "Testing mode-coupling theory for a supercooled binary Lennard-Jones mixture I: The van Hove correlation function." *Phys. Rev. E* **1995**, *51*, 4626.

[86] Wahnström, G. "Molecular-dynamics study of a supercooled two-component Lennard-Jones system." *Phys. Rev. A* **1991**, *44*, 3752–3764.

[87] Allen, M. P.; Tilesley, D. J. *Computer Simulation of Liquids*; Clarendon: Oxford, 1987.

[88] Elmatad, Y. S.; Chandler, D.; Garrahan, J. P. "Corresponding States of Structural Glass Formers." *J. Phys. Chem. B* **2009**, *113*, 5563–5567.

[89] Elmatad, Y. S.; Chandler, D.; Garrahan, J. P. "Corresponding States of Structural Glass Formers. II." *J. Phys. Chem. B* **2010**, *114*, 17113–17119.

[90] Wang, G.; Zhang, L.; Zhang, J. "A Review of Electrode Materials for

Electrochemical Supercapacitors." *Chem. Soc. Rev.* **2012**, *41*, 797–828.

[91] Pinilla, C.; Del Pópolo, M. G.; Kohanoff, J.; Lynden-Bell, R. M. "Polarization Relaxation in an Ionic Liquid Confined Between Electrified Walls." *J. Phys. Chem. B* **2007**, *111*, 4877–4884.

[92] Kornyshev, A. A. "Double-Layer in Ionic Liquids: Paradigm Change?" *J. Phys. Chem. B* **2007**, *111*, 5545–5557.

[93] Kislenko, S. A.; Samoylov, I. S.; Amirov, R. H. "Molecular Dynamics Simulation of the Electrochemical Interface Between a Graphite Surface and the Ionic Liquid [BMIM][PF_6]." *Phys. Chem. Chem. Phys.* **2009**, *11*, 5584–5590.

[94] Frackowiak, E. "Carbon materials for supercapacitor application." *Phys. Chem. Chem. Phys.* **2007**, *9*, 1774–1785.

[95] Li, S.; Zhang, P.; Pasquale, F. F.; Patrick, C. H.; Feng, G.; Dai, S.; Peter, T. C. "Enhanced performance of dicationic ionic liquid electrolytes by organic solvents." *J. Phys.: Condens. Matter* **2014**, *26*, 284105.

[96] Chaban, V. V.; Voroshylova, I. V.; Kalugin, O. N.; Prezhdo, O. V. "Acetonitrile Boosts Conductivity of Imidazolium Ionic Liquids." *J. Phys. Chem. B* **2012**, *116*, 7719–7727.

[97] Lota, K.; Khomenko, V.; Frackowiak, E. "Capacitance properties of poly(3,4-ethylenedioxythiophene)/carbon nanotubes composites." *J. Phys. Chem. Solids* **2004**, *65*, 295–301.

[98] Shim, Y.; Jung, Y.; Kim, H. J. "Graphene-Based Supercapacitors: A Computer Simulation Study." *J. Phys. Chem. C* **2011**, *115*, 23574–23583.

[99] Shim, Y.; Kim, H. J.; Jung, Y. "Graphene-Based Supercapacitors in the Parallel-Plate Electrode Configuration: Ionic Liquids versus Organic Electrolytes." *Faraday Discuss.* **2012**, *154*, 249–263.

[100] Shim, Y.; Jung, Y.; Kim, H. J. "Correction to Graphene-Based Supercapacitors: A Computer Simulation Study." *J. Phys. Chem. C* **2012**, *116*, 18574–18575.

[101] Brownson, D. A. C.; Kampouris, D. K.; Banks, C. E. "An Overview of Graphene in Energy Production and Storage Applications." *J. Power Sources* **2011**, *196*, 4873–4885.

[102] Huang, X.; Zeng, Z.; Fan, Z.; Liu, J.; Zhang, H. "Graphene-Based Electrodes." *Adv. Mater.* **2012**, *24*, 5979–6004.

[103] Merlet, C.; Rotenberg, B.; Madden, P. A.; Taberna, P.-L.; Simon, P.; Gogotsi, Y.; Salanne, M. "On the Molecular Origin of Supercapacitance in Nanoporous Carbon Electrodes." *Nature Mater.* **2012**, *11*, 306–310.

[104] Vatamanu, J.; Cao, L.; Borodin, O.; Bedrov, D.; Smith, G. D. "On the Influence of Surface Topography on the Electric Double Layer Structure and Differential Capacitance of Graphite/Ionic Liquid Interfaces." *J. Phys. Chem. Lett.* **2011**, *2*, 2267–2272.

[105] Vatamanu, J.; Borodin, O.; Smith, G. D. "Molecular Dynamics Simulation Studies of the Structure of a Mixed Carbonate/$LiPF_6$ Electrolyte Near Graphite Surface as a Function of Electrode Potential." *J. Phys. Chem. C* **2012**, *116*, 1114–1121.

[106] Vatamanu, J.; Borodin, O.; Bedrov, D.; Smith, G. D. "Molecular Dynamics Simulation Study of the Interfacial Structure and Differential Capacitance of Alkylimidazolium Bis(trifluoromethanesulfonyl)imide [$C_n$mim][TFSI] Ionic Liquids at Graphite Electrodes." *J. Phys. Chem. C* **2012**, *116*, 7940–7951.

[107] Ue, M.; Takeda, M. "Application of Ionic Liquids Based on 1-Ethyl-3-Methylimidazolium Cation and Fluoroanions to Double-Layer Capacitors." *J. Korean Electrochem. Soc.* **2002**, *5*, 192.

[108] Sato, T.; Masuda, G.; Takagi, K. "Electrochemical properties of novel ionic liquids for electric double layer capacitor applications." *Electrochimica Acta* **2004**, *49*, 3603–3611.

[109] Garcia, B.; Lavallée, S.; Perron, G.; Michot, C.; Armand, M. "Room temperature molten salts as lithium battery electrolyte." *Electrochim. Acta* **2004**, *49*, 4583–4588.

[110] Liu, C.; Yu, Z.; Neff, D.; Zhamu, A.; Jang, B. Z. "Graphene-Based Supercapacitor with an Ultrahigh Energy Density." *Nano Letters* **2010**, *10*, 4863–4868, PMID: 21058713.

[111] Shi, M.; Kou, S.; Yan, X. "Engineering the Electrochemical Capacitive Properties of Graphene Sheets in Ionic-Liquid Electrolytes by Correct Selection of Anions." *ChemSusChem* **2014**, *7*, 3178–3178.

[112] Mattevi, C.; Eda, G.; Agnoli, S.; Miller, S.; Mkhoyan, K. A.; Celik, O.; Mastrogiovanni, D.; Granozzi, G.; Garfunkel, E.; Chhowalla, M. "Evolution of electrical, chemical, and structural properties of transparent and conducting chemically derived graphene thin films." *Adv. Funct. Mater.* **2009**, *19*, 2577–2583.

[113] Hantel, M. M.; Kaspar, T.; Nesper, R.; Wokaun, A.; Kötz, R. "Partially Reduced Graphite Oxide for Supercapacitor Electrodes: Effect of Graphene Layer Spacing and Huge Specific Capacitance." *Electrochem. Commun.* **2011**, *13*, 90–92.

[114] Hantel, M. M.; Kaspar, T.; Nesper, R.; Wokaun, A.; Kötz, R. "Partially Reduced Graphite Oxide as an Electrode Material for Electrodchemical Double-Layer Capacitors." *Chem. Eur. J.* **2012**, *18*, 9125–9136.

[115] Hantel, M. M.; Płatek, A.; Kaspar, T.; Nesper, R.; Wokaun, A.; Kötz, R. "Investigation of diluted ionic liquid 1-ethyl-3-methylimidazolium tetrafluoroborate electrolytes for intercalation-like electrodes used in supercapacitors." *Electrochim. Acta* **2013**, *110*, 234–239.

[116] Kerisit, S.; Schwenzer, B.; Vijayakumar, M. "Effects of Oxygen-Containing Functional Groups on Supercapacitor Performance." *J. Phys. Chem. Lett.* **2014**, *5*, 2330–2334.

[117] Xu, K.; Ji, X.; Chen, C.; Wan, H.; Miao, L.; Jiang, J. "Electrochemical double layer near polar reduced graphene oxide electrode: Insights

from molecular dynamic study." *Electrochim. Acta* **2015**, *166*, 142–149.

[118] Dreyer, D. R.; Park, S.; Bielawski, C. W.; Ruoff, R. S. "The Chemistry of Graphene Oxide." *Chem. Soc. Rev.* **2010**, *39*, 228–240.

[119] Compton, O. C.; Nguyen, S. T. "Graphene Oxide, Highly Reduced Graphene Oxide, and Graphene: Versatile Building Blocks for Carbon-Based Materials." *Small* **2010**, *6*, 711–723.

[120] Paci, J. T.; Belytschko, T.; Schatz, G. C. "Computational Studies of the Structure, Behavior upon Heating, and Mechanical Properties of Graphite Oxide." *J. Phys. Chem. C* **2007**, *111*, 18099–18111.

[121] Boukhvalov, D. W.; Katsnelson, M. I. "Modeling of Graphite Oxide." *J. Am. Chem. Soc.* **2008**, *130*, 10697–10701.

[122] Li, Z.; Zhang, W.; Luo, Y.; Yang, J.; Hou, J. G. "How Graphene is Cut upon Oxidation?" *J. Am. Chem. Soc.* **2009**, *131*, 6320–6321.

[123] Lahaye, R. J. W. E.; Jeong, H. K.; Park, C. Y.; Lee, Y. H. "Density Functional Theory Study of Graphite Oxide for Different Oxidation Levels." *Phys. Rev. B* **2009**, *79*, 125435.

[124] Zhang, W.; Carravetta, V.; Li, Z.; Luo, Y.; Yang, J. "Oxidation States of Graphene: Insights from Computational Spectroscopy." *J. Chem. Phys.* **2009**, *131*, 244505.

[125] Lu, N.; Huang, Y.; Li, H.-b.; Li, Z.; Yang, J. "First Principles Nuclear Magnetic Resonance Signatures of Graphene Oxide." *J. Chem. Phys.* **2010**, *133*, 034502.

[126] Yin, D.; Lu, N.; Li, Z.; Yang, J. "A Computational Infrared Spectroscopic Study of Graphene Oxide." *J. Chem. Phys.* **2013**, *139*, 084704.

[127] Jorgensen, W. L.; Maxwell, D. S.; Tirado-Rives, J. "Development and Testing of the OPLS All-Atom Force Field on Conformational Energetics and Properties of Organic Liquids." *J. Am. Chem. Soc.* **1996**, *118*, 11225–11236.

[128] Hummer, G.; Rasaiah, J. C.; Noworyta, J. P. "Water Conduction through the Hydrophobic Channel of a Carbon Nanotube." *Nature* **2001**, *414*, 188–190.

[129] Canongia Lopes, J. N.; Deschamps, J.; Pádua, A. A. H. "Modeling Ionic Liquids Using a Systematic All-Atom Force Field." *J. Phys. Chem. B* **2004**, *108*, 11250–11250.

[130] de Andrade, J.; Böes, E. S.; Stassen, H. "Computational Study of Room Temperature Molten Salts Composed by 1-Alkyl-3-methylimidazolium CationsForce-Field Proposal and Validation." *J. Phys. Chem. B* **2002**, *106*, 13344–13351.

[131] Wu, X.; Liu, Z.; Huang, S.; Wang, W. "Molecular dynamics simulation of room-temperature ionic liquid mixture of [bmim][BF4] and acetonitrile by a refined force field." *Phys. Chem. Chem. Phys.* **2005**, *7*, 2771–2779.

[132] Nikitin, A. M.; Lyubartsev, A. P. "New Six-Site Acetonitrile Model for Simulations of Liquid Acetonitrile and Its Aqueous Mixtures." *J. Comput. Chem.* **2007**, *28*, 2020.

[133] Pronk, S.; Páll, S.; Schulz, R.; Larsson, P.; Bjelkmar, P.; Apostolov, R.; Shirts, M. R.; Smith, J. C.; Kasson, P. M.; van der Spoel, D.; Hess, B.; Lindahl, E. "GROMACS 4.5: a high-throughput and highly parallel open source molecular simulation toolkit." *Bioinformatics* **2013**, *29*, 845–854.

[134] Yeh, I.-C.; Berkowitz, M. L. "Ewald Summation for Systems with Slab Geometry." *J. Chem. Phys.* **1999**, *111*, 3155–3162.

[135] Lynden-Bell, R. M.; Frolov, A. I.; Fedorov, M. V. "Electrode screening by ionic liquids." *Phys. Chem. Chem. Phys.* **2012**, *14*, 2693–2701.

[136] Griffin, J. M.; Forse, A. C.; Wang, H.; Trease, N. M.; Taberna, P.-L.; Simon, P.; Grey, C. P. "Ion counting in supercapacitor electrodes using NMR spectroscopy." *Faraday Discuss.* **2014**, *176*, 49–68.

[137] Shim, Y.; Kim, H. J. "Nanoporous Carbon Supercapacitors in an Ionic Liquid: A Computer Simulation Study." *ACS Nano* **2010**, *4*, 2345–2355.

[138] Vatamanu, J.; Hu, Z.; Bedrov, D.; Perez, C.; Gogotsi, Y. "Increasing Energy Storage in Electrochemical Capacitors with Ionic Liquid Electrolytes and Nanostructured Carbon Electrodes." *J. Phys. Chem. Lett.* **2013**, *4*, 2829–2837.

[139] Xing, L.; Vatamanu, J.; Smith, G. D.; Bedrov, D. "Nanopatterning of Electrode Surfaces as a Potential Route to Improve the Energy Density of Electric Double-Layer Capacitors: Insight from Molecular Simulations." *J. Phys. Chem. Lett.* **2012**, *3*, 1124–1129.

국문초록

이온성 액체는 양이온과 음이온만으로 이루어진 유기용매이다. 양이온은 크고 복잡한 분자구조를 갖기 때문에 상온에서도 액체로 존재한다. 이 논문에서는 분자동역학 시뮬레이션 방법을 통하여 이온성 액체의 동역학적 특성 중 과냉각 액체로서의 특성인 동역학적 불균일성과 이온성 액체가 전해질로 사용된 초고용량 축전기(supercapacitor)에 대한 응용적인 측면을 연구하였다.

먼저, 이온성 액체 분자 안의 전하분포와 거리척도에 따라 동역학적 불균일성이 어떻게 변화하는 지 연구하였다. 다른 전하분포를 갖는 이온성 액체 모형 두 가지와 구조는 같고 전하가 제거된 모형을 도입하여 전하 분포에 따른 차이를 확인한다. 한 이온성 액체 모형(대칭전하모형, SCM)에는 전하가 고루 분포하고, 다른 모형(비대칭전하모형, ACM)에는 전하가 한 쪽에만 분포한다. 모든 모형에서 불균일한 동역학적 동태를 보임을 확인하였다. 동역학적 불균일성은 유리상 전이를 이해하는 데 중요한 역할을 하는데, 이 연구에서는 네시점상관함수를 도입하여 동역학적 불균일성의 시간척도(τ_{dh})를 이온성 액체에서는 처음으로 정량적으로 계산하였다. 동역학적 불균일성의 시간척도가 구조완화시간(τ_α)과 보편적인 거듭제곱 법칙($\tau_{\mathrm{dh}} \propto \tau_\alpha^{\zeta_{\mathrm{dh}}}$)을 보이며, 확산과정과 탈결합 현상을 보인다. 비대칭전하모형이 겉보기에 동역학적으로 더 불균일한 것처럼 보이나, 거듭제곱 법칙의 지수(ζ_{dh})가 모든 모형에서 동일한 값(1.2)을 갖는다. 이에 따라 정전기적 상호작용보다 근거리 상호작용에 좌

우됨을 확인하였다. 뿐만 아니라, 거리척도에 대해서도 이 거듭제곱 법칙은 일정하게 유지되어 Fick의 법칙이 성립하는 거리척도에서도 동역학적 불균일성이 사라지지 않는 특이한 결과를 발견하였다.

또한, 이온성 액체 전해질과 산화그래핀 전극으로 이루어진 초고용량 축전기의 물성을 연구하였다. 전기이중층 축전기, 또는 초고용량 축전기는 높은 전력밀도와 적당한 에너지밀도를 갖는 에너지 저장장치이다. 이 논문에서는 평행한 산화그래핀 전극 사이에 아세토니트릴에 이온성 액체가 섞인 전해질이 있는 전기이중층 축전기 모형으로부터 그래핀의 산화도와 전해질의 종류에 따라 축전용량과 같은 특성이 달라지는 원인이 분자 수준의 상호작용에 있고, 특히 수소결합이 중요한 역할을 함을 규명하였다.

주요어: 이온성 액체, 동역학적 불균일성, 유리 동역학, 전기이중층, 초고용량 축전기, 산화그래핀

학번: 2008-20323